Open Research Online

The Open University's repository of research publications
and other research outputs

TIC 278956474: Two Close Binaries in One Young Quadruple System Identified by TESS

Journal Item

oro.open.ac.uk

TIC 278956474: Two close binaries in one young quadruple system, identified by *TESS*

Pamela Rowden,[1] Tamás Borkovits,[2,3] Jon M. Jenkins,[4] Keivan G. Stassun,[5,6] Joseph D. Twicken,[4,7]
Elisabeth R. Newton,[8] Carl Ziegler,[9] Coel Hellier,[10] Aylin Garcia Soto,[8] Elisabeth C. Matthews,[11]
Ulrich Kolb,[1] George R. Ricker,[11] Roland Vanderspek,[11] David W. Latham,[12] S. Seager,[11,13,14]
Joshua N. Winn,[15] Luke G. Bouma,[15] César Briceño,[16] David Charbonneau,[12] William Fong,[11] Ana Glidden,[13,11]
Natalia M. Guerrero,[11] Nicholas Law,[17] Andrew W. Mann,[17] Mark E. Rose,[4] Joshua Schlieder,[18]
Peter Tenenbaum,[7,4] and Eric B. Ting[4]

[1] *School of Physical Sciences, The Open University, Milton Keynes MK7 6AA, UK*
[2] *Baja Astronomical Observatory of Szeged University, H-6500 Baja, Szegedi t, kt. 766, Hungary*
[3] *Konkoly Observatory, Research Centre for Astronomy and Earth Sciences, H-1121 Budapest, Konkoly Thege Mikls t 15-17, Hungary*
[4] *NASA Ames Research Center, Moffett Field, CA, 94035, USA*
[5] *Department of Physics and Astronomy, Vanderbilt University, Nashville, TN 37235, USA*
[6] *Department of Physics, Fisk University, Nashville, TN 37208, USA*
[7] *SETI Institute, Mountain View, CA 94043, USA*
[8] *Department of Physics and Astronomy, Dartmouth College, Hanover, NH, 03755, USA*
[9] *Dunlap Institute for Astronomy and Astrophysics, University of Toronto, 50 St. George Street, Toronto, Ontario M5S 3H4, Canada*
[10] *Astrophysics Group, Keele University, Staffordshire, ST5 5BG, UK*
[11] *Department of Physics and Kavli Institute for Astrophysics and Space Research, Massachusetts Institute of Technology, Cambridge, MA 02139, USA*
[12] *Center for Astrophysics | Harvard & Smithsonian, 60 Garden Street, Cambridge, MA 02138, USA*
[13] *Department of Earth, Atmospheric and Planetary Sciences, Massachusetts Institute of Technology, Cambridge, MA 02139, USA*
[14] *Department of Aeronautics and Astronautics, MIT, 77 Massachusetts Avenue, Cambridge, MA 02139, USA*
[15] *Department of Astrophysical Sciences, Princeton University, 4 Ivy Lane, Princeton, NJ 08544, USA*
[16] *Cerro Tololo Inter-American Observatory, Casilla 603, La Serena, Chile*
[17] *Department of Physics and Astronomy, The University of North Carolina at Chapel Hill, Chapel Hill, NC 27599-3255, USA*
[18] *NASA Goddard Space Flight Center, 8800 Greenbelt Rd, Greenbelt, MD 20771, USA*

ABSTRACT

We have identified a quadruple system with two close eclipsing binaries in *TESS* data. The object is unresolved in Gaia and appears as a single source at parallax 1.08 ±0.01 mas. Both binaries have observable primary and secondary eclipses and were monitored throughout *TESS* Cycle 1 (sectors 1-13), falling within the *TESS* Continuous Viewing Zone. In one eclipsing binary ($P = 5.488$ d), the smaller star is completely occluded by the larger star during the secondary eclipse; in the other ($P = 5.674$ d) both eclipses are grazing. Using these data, spectroscopy, speckle photometry, SED analysis and evolutionary stellar tracks, we have constrained the masses and radii of the four stars in the two eclipsing binaries. The Li I EW indicates an age of 10-50 Myr and, with an outer period of 858^{+7}_{-5} days, our analysis indicates this is one of the most compact young 2+2 quadruple systems known.

Keywords: binaries: close – binaries: eclipsing

1. INTRODUCTION

The main purpose of the Transiting Exoplanet Survey Satellite, *TESS* (Ricker et al. 2014), is to identify nearby planets ≤ 4 R$_\oplus$ which can be fully characterised. However, a great deal of complementary science has come from the mission, particularly in stellar science (see for example Fausnaugh et al. (2019), Holoien et al. (2019),

Corresponding author: Pamela Rowden
pam.rowden27@gmail.com

Huber et al. (2019); Schofield et al. (2019), Zhan et al. (2019), Ahlers et al. (2020)).

Eclipsing binaries are known to be detected in transiting exoplanet surveys. $\approx$ 16% of *Kepler* Objects of Interest (KOIs) have been identified by the *Kepler* pipeline as eclipsing binaries, and a further $\approx$7% as background eclipsing binaries[1]. Moreover, the *Kepler* and *K2* missions have also identified triple and quadruple eclipsing systems and even a bound quintuple system (KOI 3156) exhibiting eclipses of at least three different subsystems (Hełminiak et al. 2017).

Raghavan et al. (2010) estimate that, among solar-type stars, 33±2% of systems are binary, 8±1% of systems are triple, 9±2% of systems are quadruple and 3±1% are composed of five stars. As an all-sky survey, *TESS* can be expected to identify a proportion of these rarer multiple star systems.

We use *TESS* data to identify a 2+2 quadruple star system (TIC 278956474) with two short-period inner binaries. We estimate the age of TIC 278956474 as 10-50 Myr (Section 2.6), making this a young system. Known young quadruple systems include GG Tauri (Guilloteau et al. 1999; Köhler 2011), HD 98800 (Tokovinin 1999; Ribas et al. 2018), HD 34700 (Sterzik et al. 2005), AB Doradus (Janson et al. 2007; Wolter et al. 2014), AO Vel (González et al. 2006, 2008b,a), HD 91962 (Tokovinin et al. 2015), LkCa 3 (Torres et al. 2013; Baraffe et al. 2015) and HD 86588 (Tokovinin et al. 2018). IRS5 might be a young quadruple system (Chen et al. 2015). LkHα 263C, around which a circumstellar disc has been identified (Jayawardhana et al. 2002), appears to be a member of a young quadruple system in the MBM 12 association.

While considering the binary population of young clusters, Marks & Kroupa (2012) demonstrated from simulations that clusters with a formal binary fraction of unity at birth will evolve to a lower binary fraction over time. They note that younger clusters appear to have a higher binary fraction than older clusters with a similar stellar density (see for example Duchêne (1999)). Thus, studying the population of young quadruple systems such as TIC 278956474 is of interest when considering the evolution of the binary fraction of stellar clusters over time.

This paper is organised as follows. In Section 2 we discuss the data. In Section 3 we present our models, which confirm that this is a young 2+2 quadruple system. The models are discussed in Section 4: in particular, we consider the dynamical properties of the system, as well as

[1] https://exoplanetarchive.ipac.caltech.edu/docs/data.html

Table 1. Basic data on TIC 278956474.

Parameter	Value
Alternative names[1]	UCAC4 165-008872
	2MASS J06454123-5708171
	WISE J064541.25-570817.0
	APASS 27316174
RA[1,2]	101.421895°
dec[1,2]	-57.138098°
l[1]	266.7396°
b[1]	-23.2743°
Parallax[2]	1,08 ± 0.01 mas
Proper motion RA[2]	4.29 ± 0.03 mas yr^{-1}
Proper motion dec[2]	-2.21 ± 0.03 mas yr^{-1}
B[1]	14.191 ± 0.052
Gaia bp[2]	13.7641
V[1]	13.542 ± 0.092
Gaia[1,2]	13.4153 ± 0.000408
TESS[1]	12.9637 ± 0.006
Gaia rp[2]	12.9020
J[1]	12.291 ± 0.022
H[1]	11.951 ± 0.024
K[1]	11.835 ± 0.021
WISE 3.4 micron[1]	11.813 ± 0.023
WISE 4.6 micron[1]	11.826 ± 0.021
WISE 12 micron[1]	12.048 ± 0.178
WISE 22 micron[1]	9.681

Sources: 1. Exofop https://exofop.ipac.caltech.edu/tess/. 2. *Gaia* DR2 https://gea.esac.esa.int/archive/.

its place among known young quadruple star systems. Our conclusions are drawn in Section 5.

2. DATA

Table 1 gives some basic data on TIC 278956474, such as alternative names, position, proper motion and magnitudes in various passbands. The data are drawn from Exofop[2], and from *Gaia* DR2[3].

2.1. *SPOC data*

Threshold crossing events (TCEs) were identified in observations of TIC 278956474 in two minute cadence data, processed by NASA's TESS Science Processing Operations Center (SPOC) (Jenkins 2019; Jenkins et al. 2016). TIC 278956474 lies in the Southern Continuous Viewing Zone (CVZ) near the Southern ecliptic pole and was observed on camera 4 throughout *TESS* Cycle 1

[2] https://exofop.ipac.caltech.edu/tess/
[3] https://gea.esac.esa.int/archive/
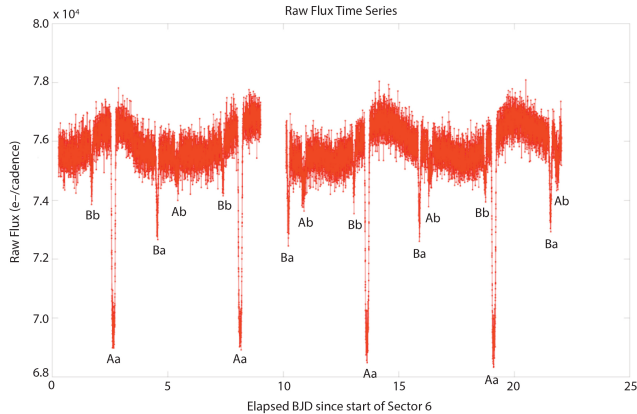
Figure 1. Simple Aperture Photometry (SAP) light curve for Sector 6, annotated to indicate the various eclipses. The start BJD for Sector 6 is 2458468. Similar raw flux light curves are available for each *TESS* sector in the range $1-13$ and are included in the publicly available data validation reports hosted on MAST.

(Sectors 1-13). We focus on the depth of each SPOC TCE in ppm.

Fig. 1 illustrates the Simple Aperture Photometry (SAP) light curve (Twicken et al. 2010; Morris et al. 2017) for sector 6, annotated to highlight the eclipses. Similar information is available on all 13 sectors, and is included in the publicly available data validation reports hosted on MAST.

Selected data on this target from SPOC data validation reports (Twicken et al. (2018), Li et al. (2019)) is presented in Table 2 (multi-sector analysis, sectors 1-13) and in Table 4 (all single sector and multi sector analyses).

The deepest eclipse and the shallowest eclipse both relate to the same binary ('A'). This binary has a period of 5.488 days. We label the two components Aa and Ab. The second binary ('B') has a period of 5.674 days, and its components are labelled Ba and Bb.

The SPOC analysis indicates that both eclipses in B are V-shaped, while both eclipses in A are U-shaped. This indicates the eclipses in B are grazing, while in A star Ab is fully occluded as it passes behind Aa. We obtain a preliminary estimate of the ratio of the radii of Ab:Aa (≈ 0.29) by comparing the ingress duration with the total eclipse duration. See Fig. 2 for a cartoon illustrating the relative radii of the four stars to scale and the proportion of each star that is occluded during an eclipse. Each pair of stars is positioned as it would be at the middle of the primary transit, given the approximate angle of inclination, as observed by TESS.

2.2. *WASP-South photometry*
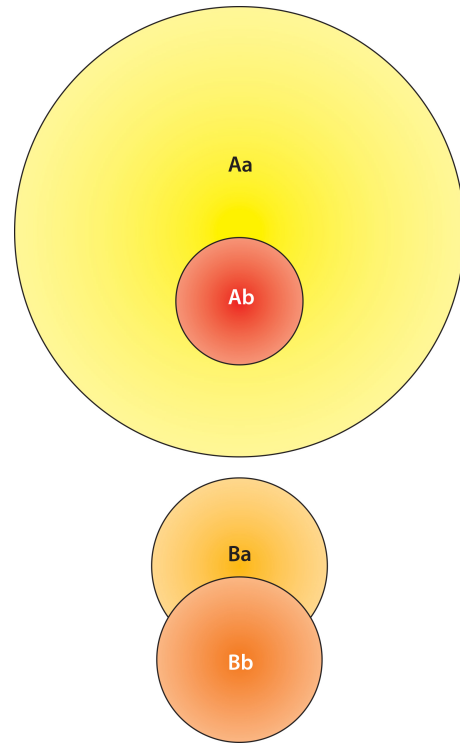
Figure 2. Cartoon showing the relative sizes of the four stars to scale and the proportions of the stars that are occluded during eclipses. Each pair of stars is positioned as it would be at the middle of the primary transit, given the approximate angle of inclination, as observed by TESS.

WASP-South was the southern station of the WASP transit-search project (Pollacco et al. 2006), situated in Sutherland, South Africa. It observed the field of TIC 278956474 for four consecutive years from 2008 September, spanning 170 nights each year, and obtaining a total of 26 700 photometric data points. The observations used 200-mm, f/1.8 lenses with a 400–700 nm passband, backed by 2048×2048 CCDs. Reduction with the WASP pipeline produced photometry relative to other stars in the field with an extraction aperture of 48". At a *Gaia* magnitude of 13.4, the star is at the faint end of the WASP range, but the data are sufficient to detect 10% eclipses.

2.3. *Period study*

One way to determine whether two eclipsing binaries producing a blended lightcurve are physically bound is to find anti-correlated eclipse timing variations (ETV) in the two pairs. Similar anti-correlated ETVs have proven the real, bound 2+2 quadruple nature of V994 Her (Lee et al. 2008; Zasche & Uhlař 2016) and EPIC 220204960 (Rappaport et al. 2017). More recently, Zasche et al. (2019) performed a thorough analysis of a larger sample of doubly eclipsing binaries found within the frame of

Table 2. Data from SPOC. The secondary in component Aa coincides with the time of the primary in component Ab, and vice versa. Similarly for components Ba and Bb. Secondary depths are therefore only included where each component is not separately identified, as is the case with B in this table, which has been identified at half the true period. A second science run was completed for multisector 1-13 in order to identify component Ab at the correct period and to remove the partial eclipse of Aa at the end of sector 8. This science run is identified as sector 1-13*. For data from each sector, see Table 4.

Component	Sector	Period/days	Depth/ppm	Duration/hr	Ingress/hr	Odd depth/ppm	Even depth/ppm	Secondary depth/ppm
Aa	1-13	5.488035 ± 0.000005	93900 ± 200	5.43 ± 0.01	1.22 ± 0.01	94600 ± 300	93300 ± 300	8900 ± 400
Aa	1-13*	5.488036 ± 0.000005	93900 ± 200	5.43 ± 0.01	1.22 ± 0.01	94500 ± 300	93400 ± 300	Component Ab
Ab	1-13	2.74403 ± 0.00002	8900 ± 200	5.29 ± 0.09	1.0 ± 0.1	Model fitter failed	Model fitter failed	n/a
Ab	1-13*	5.48808 ± 0.00004	8900 ± 200	5.29 ± 0.08	1.0 ± 0.1	9000 ± 300	8700 ± 300	Component Aa
B	1-13	2.837163 ± 0.000007	25100 ± 200	3.34 ± 0.03	1.67 ± 0.02	16400 ± 300	33400 ± 300	n/a
B	1-13*	2.837162 ± 0.000007	25100 ± 200	3.34 ± 0.03	1.67 ± 0.02	16400 ± 200	33400 ± 300	n/a

the several year-long photometry of the Optical Gravitational Lensing Experiment (OGLE) survey (Udalski et al. 2015), and identified 28 systems where the ETVs showed evidence of light-travel time effect caused by the relative motion of the two binaries around their common center of mass and/or perturbations due to the dynamical interactions of the two binaries. To search for ETVs in the two eclipsing binaries in TIC 278956474, we determined the times of minimum light of each eclipse observed with *TESS* in the same manner as was described in Section 5 of Borkovits et al. (2018).

In summary, after removing the eclipses of the other binary the light curves were phase folded, binned into 1000 equally phased cells, and averaged within each cells. In this way we obtained distentangled, phase folded light curves for both binaries (see Fig. 3). Then, the eclipses of these light curves were fitted with 8–10th order polynoms, and in this way we obtained separate templates for both the primary and secondary eclipses. Then these templates were fitted to each individual eclipse events. (Naturally, we excluded those events which were affected by any eclipses of the other binary.) We obtained $\sim 4 \times 50$ separate minima times (primary and secondary eclipses for both systems) (Tables 5 and 6). In what follows, however, we concentrate only on the ETVs of the two primary eclipses, as the secondary ETV points, determined from shallower eclipses, have much higher scatter.

We also took into account the historical WASP-South observations (see Section 2.2). These data have large scatter, and therefore, are unsuitable for determining individual eclipse times. However, folding these measurements with the period of binary A season by season, we were able to determine additional seasonal primary minimum times for binary A with a reasonable accuracy. These four seasonal minima are also tabulated in Tables 5 and 6.

We plot the ETVs of the primary eclipses of both binaries in the two panels of Fig. 4. The anti-correlated nature of the non-linear timing variations of both bina-

ries are clearly visible. The most likely origin of this feature is the light-travel time effect (LTTE) which arises from the varying distances of the two binaries from the Earth during their revolution around the common center of mass of the whole quadruple system. Therefore, the ETVs strongly suggest that TIC 278956474 is one of the tightest known physically bound 2+2 quadruple systems. This question will be discussed further in Section 3.2.

2.4. *Gaia DR2*

TIC 278956474 was identified by *Gaia* (Gaia Collaboration et al. 2016, 2018; Riello et al. 2018; Andrae et al. 2018) as a single source with a mean *Gaia* magnitude of 13.4 and a parallax of 1.08 ± 0.01 mas, corresponding to a distance of 926 ± 12 pc. Various systematic corrections to *Gaia* parallaxes have been proposed. The online documentation for *Gaia* DR2 states a correction of -0.03 mas may be appropriate. The probabilistically derived distance in Bailer-Jones et al. (2018) indicates a distance of 903^{+12}_{-9} pc for TIC 278956474, which corresponds to an offset of -0.03 mas. Schönrich et al. (2019) finds that on average the parallax offset is -0.054 mas; while Stassun & Torres (2018) find evidence for a systematic offset of -0.082 ± 0.033 mas, for brightnesses G ≥ 12 and for distances 0.03-3 kpc. All agree that *Gaia* parallaxes as recorded in the data releases are too small. Despite this, our best fit model (Section 3.2) indicates that the uncorrected *Gaia* parallax for this system is slightly too large and that the true distance is 958 ± 23 pc.

Gaia DR2 assigns a Renormalised Unit Weight Error (RUWE) to each source, where a value of 1.0 indicates the source is likely to be a single star, and a value $\geq$ 1.4 indicates that a source is likely to be non-single or otherwise problematic for the astrometric solution, for example a $\leq 1''$ binary. The RUWE for TIC 278956474 is 1.06. However, we know from the *TESS* data that TIC 278956474 is a 2+2 quadruple system, not a single star. The low Gaia DR2 RUWE value suggests the two binaries are likely to be tightly bound.
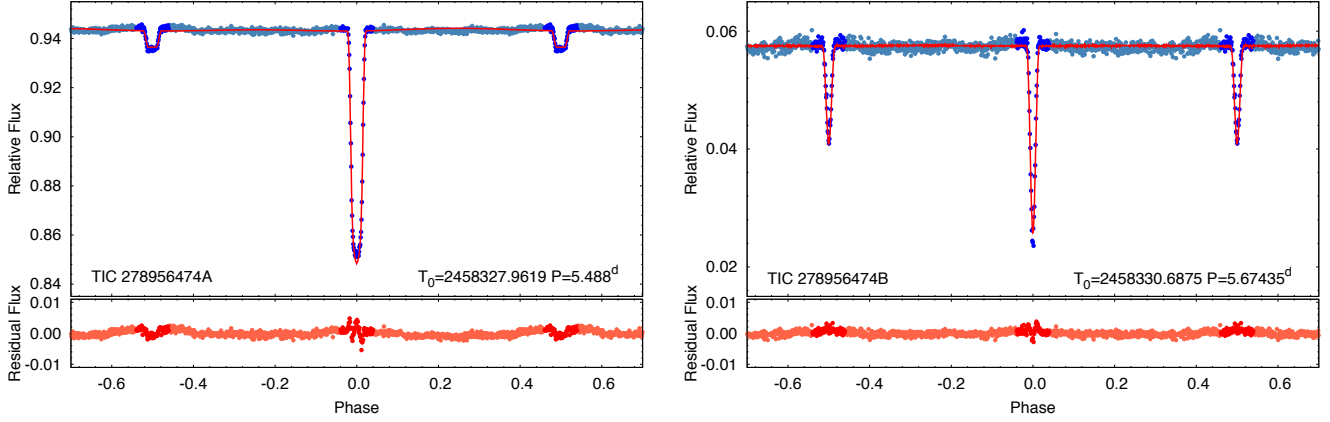
Figure 3. The disentangled, phase-folded, binned, averaged light curves (blue points) of binaries A (left) and B (right), together with the complex model solution light curves (see below, in Sect. 3.2), processed in the same manner. (For the joint analysis only the darker blue points were used.) The lowest, residual data were also obtained with phase-folding, binning and averaging the residual curve of the complete light curve model.
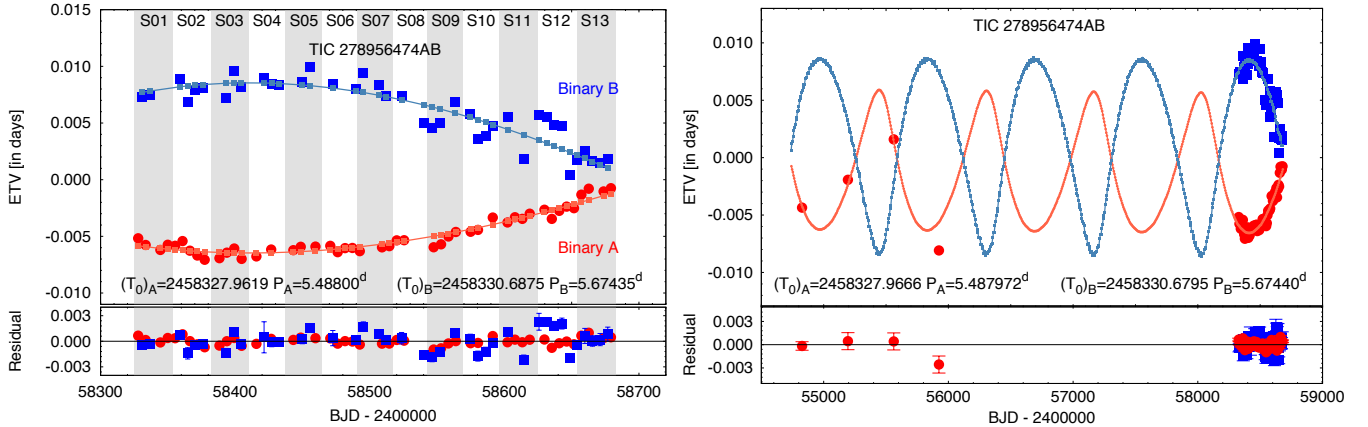
Figure 4. Eclipse Timing Variations of the primary minima of TIC 278956474A and B (red and blue, respectively). The anti-correlated nature of the nonlinear timing variations, most likely due to the light-travel time effect, occurs due to the revolution of the barycentres of the two binaries around the common center of mass of the quadruple. Lighter red and blue lines represent the model solutions obtained through the combined light-, ETV and RV-curve analysis, discussed in Section 3.2. Left panel displays the ETVs during the first year of *TESS* observations, whilst the four earlier primary minima of binary A derived from the seasonal average light curves of the historical WASP-South observations are also plotted in the right panel.

Gaia DR2 does not specify an extinction for this system. We use several sources to estimate extinction in the *Gaia* passband. From the catalogue Lallement et al. (2019), which uses Gaia and 2MASS photometric data to estimate the extinction toward 27 million carefully selected target stars with a Gaia DR2 parallax uncertainty below 20%, we estimate the extinction at 0.196 in the *Gaia* passband, although it should be noted that the region in question falls outside the edges of the dust map and hence the reddening is estimated.

Dust maps from Schlegel et al. (1998) indicate the extinction in the V band along the line of sight is $0.198 \leq A_V \leq 0.224$ (mean 0.212 ± 0.007), and dust maps from Schlafly & Finkbeiner (2011) indicate the extinc-

tion along the line of sight is $0.170 \leq A_V \leq 0.193$ (mean 0.182 ± 0.002).

An online tool[4] estimating N_{H1} and N_{H2} from 493 afterglows detected by the *Swift* X-Ray Telescope (Willingale et al. 2013) returns $N_{\mathrm{H,tot}}$ 7.76×10^{20} atoms cm^{-2} (mean), 7.34×10^{20} atoms cm^{-2} (weighted). Using the relation between N_H and A_V in Güver & Özel (2009), A_V is 0.35 ± 0.01 (mean), 0.33 ± 0.01 (weighted).

This is higher than other estimates, but is in line with the findings in our model of E(B-V) = $0.108^{+0.025}_{-0.012}$ mag (Section 3.2).

---

[4] https://www.swift.ac.uk/analysis/nhtot/index.php
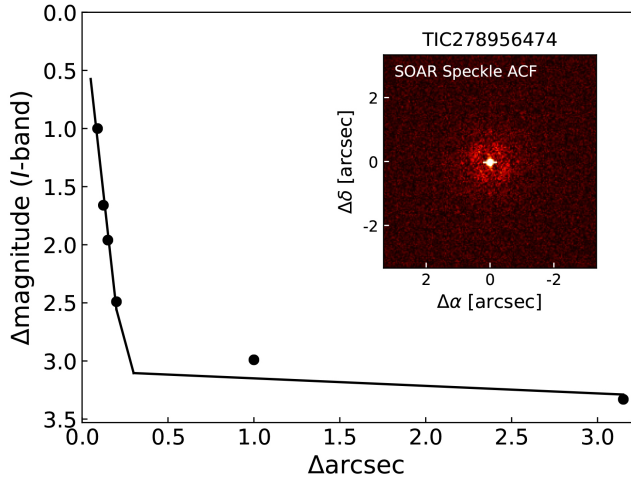
Figure 5. Speckle imaging auto-correlation function (inset) and resulting contrast curve obtained on 2020 January 07 with speckle imaging on the 4.1 m Southern Astrophysical Research (SOAR) telescope. This observation places an upper limit for the projected separation of the binaries at approximately 115 AU.

2.5. *Speckle photometry*

If the pair of binaries is widely separated, high-angular resolution imaging may be able to resolve the system or detect additional nearby stars. We searched for stellar companions to TIC 278956474 with speckle imaging on the 4.1 m Southern Astrophysical Research (SOAR) telescope (Tokovinin 2018) on 2020 January 07 UT, observing in a similar visible bandpass as *TESS*. More details of the observations are available in Ziegler et al. (2020). The 5σ detection sensitivity and speckle auto-correlation functions from the observations are shown in Fig. 5. The seeing during the night was below average, resulting in a shallow detection curve, and the binaries, assuming a $\Delta_m = 2$ in the *TESS* bandpass, would likely be resolved at angular separations greater than approximately $0.12''$, corresponding to a projected separation of ~ 115 AU at the estimated distance to the system, based on the uncorrected stellar parallax. No nearby stars, however, were detected within $3''$ of TIC 278956474, placing an upper limit for projected separations of the binaries at approximately 115 AU.

Points that appear a little less than $1''$ East, West, North, and South of the target are artefacts of the data.

The TESS Input Catalogue (TIC) identifies a 19th magnitude star $11.48''$ from the target, $106.63°$ E of N, and a 17th magnitude star $15.77''$ from the target, $141.72°$ E of N. Both these stars were also observed by *Gaia*, and *Gaia* does not identify any other stars that are closer. From the difference images in the SPOC data
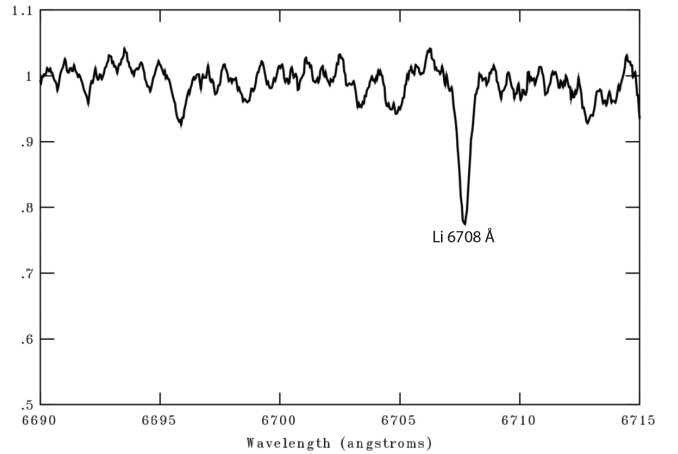
Figure 6. Spectra obtained on the High Resolution Spectrograph on the South African Extremely Large Telescope (SALT) indicate a LI 6708 Å equivalent width of 143 ±10 mÅ for the whole system.

validation reports, it is highly unlikely that the eclipses analyzed here arise from these known near neighbours.

2.6. *Spectroscopy*

We obtained two spectra using the High Resolution Spectrograph (RSS Crause et al. 2014) on the South African Extremely Large Telescope (SALT; Buckley et al. 2006). We obtained spectra on the nights of 2019 October 03 and 04. The spectra were reduced using the MIDAS pipeline (Kniazev et al. 2016, 2017)[5]. The wavelength calibration used ThAr and Ar lamps. The resulting resolution is about 46 000 and the spectra span 370 to 980 nm.

Separating the components in the spectra is challenging. The second brightest component (Ba) contributes only a few percent of the total light in the optical and any attempt to disentangle the Aa and Ba would be complicated by the presence of the two fainter components, Ab and Bb. We do note absorption of Hα and Hβ, as well as Ca II at ≈ 8664 and 8545 Å. These features are consistent with our model of the brightest star (Section 3.2).

We also identified a clear and strong Li absorption feature at 6708 Å (Fig. 6). The average equivalent width (EW) is 143 ±10 mÅ. This is almost entirely due to star Aa: the next most significant star, Ba, contributes $\approx 3\%$ of the light.

By comparison with Fig. 4 of Aarnio et al. (2008), this EW in a star of the T_{eff} of Aa (6180 K: Section 3.2) is consistent with an age of 30-50 Myr, and by comparison

---

[5] http://www.saao.ac.za/~akniazev/pub/HRS_MIDAS/HRS_pipeline.pdf

with Fig. 5 of Mentuch et al. (2008), with stars in the β Pictoris moving group (21 ± 9 Myr (Mentuch et al. 2008), 22±6 Myr (Shkolnik et al. 2017), 24±3 Myr (Bell et al. 2015)) and the Tucanae-Horologium association (isochronal age 20 − 30 Myr (Kraus et al. 2014), 28 ± 11 Myr (Mentuch et al. 2008), Li depletion age ≈ 40 Myr (Kraus et al. 2014), 45 ± 4 Myr (Bell et al. 2015)).

Estimating $V − K$ for star Aa using the $T_{\rm eff}$, distance and extinction from our model (Section 3.2), we referred to Riedel et al. (2017), which considered the Li depletion (Fig. 21) and ages (Table 1 and references therein) of stars in nearby young moving groups (NYMG). This indicates that TIC 278956474 is likely to be younger than AB Doradus (50-150 Myr), Carina-Near (150-250 Myr) and Ursa Major (300-500 Myr); older than ε Chamaeleontis (5-8 Myr), η Chamaeleontis (6-11 Myr) and TW Hydrae (3-15 Myr); and consistent with stars in the following NYMG: β Pictoris (10-24 Myr), Octans (20-40 Myr), Tucana-Horologium (30-45 Myr) and Argus (35-50 Myr).

From the Li I EW, we therefore estimate the age of the system to be 10-50 Myr.

In Fig. 6 the Li 6708Å feature has been Doppler shifted to its rest wavelength. Relative to the rest wavelength, the heliocentric RVs are 75.2 ± 1.8 km s^{-1} on the first night and 36.7 ± 2.2 km s^{-1} on the second night.

3. MODELS

3.1. *Preliminary estimates*

We made preliminary estimates of the properties of the stars in the system as follows.

Component Ab is fully occluded when it passes behind Aa. *Gaia* obtained 191 astrometric observations of the system, of which 189 were considered good and two bad. Considering that both binaries would have been out of transit for about 86% of the observing time, and that the difference between the *TESS* magnitude T and the *Gaia* magnitude in the red passband G_{BP} is only 0.06 magnitudes and that generally $T \approx G_{BP}$, it is likely that the magnitude of the system in the G passband (300-1100 nm) reflects the out-of-transit magnitude of the system. The luminosity of Ab in the *Gaia* passband can therefore be estimated from the total luminosity of the system, taking into account the *Gaia* magnitude, the *Gaia* parallax and an appropriate estimate of extinction (Section 2.4). The luminosity of Ab was estimated as as $0.0247^{+0.006}_{-0.005}$ L$_\odot$ using the correction from Stassun & Torres (2018), and $0.0279^{+0.008}_{-0.007}$ L$_\odot$ using the uncorrected *Gaia* parallax, in both cases using A$_G$ from Lallement et al. (2019).

We used a library of single star evolutionary models from the BiSEPS Binary Stellar Evolution Population

Synthesis code (Willems & Kolb 2002, 2004; Willems et al. 2006; Davis et al. 2010; Farmer et al. 2013) to approximate the likely radius, mass, effective temperature and age of Ab, assuming solar metallicity. This allowed us to eliminate the possibility that Ab was a white dwarf.

Comparing the ingress with the total eclipse time during the primary eclipse of A indicated that the ratio of the radii of the two stars was likely to be of the order of 0.29, which indicated that Aa was not evolved and was further confirmation that neither star was a white dwarf. From this and the relationship between the luminosity of Aa and Ab in the *TESS* passband (600-1000 nm centred on 786.5 nm), we estimated the radius and bolometric luminosity of Aa, also at solar metallicity.

We then used stellar evolution tracks from MESA (Modules for Experiments in Stellar Astrophysics) (Paxton et al. 2011, 2013, 2015) to refine our parameters for Aa and Ab, again assuming solar metallicity. From this we estimated the initial mass and T$_{eff}$ of Aa as 1.315 M$_\odot$ and 6456 K respectively: these estimates would be used as the starting point for the more in depth analysis described in Section 3.2, which makes use of the PARSEC (PAdova and TRieste Stellar Evolution Code) (Bressan et al. 2012) stellar evolutionary tracks.

BiSEPS evolves both single stars and binary systems self-consistently from formation to compact remnant. While not a full stellar evolutionary code, the library of models this code produces was useful in obtaining 'ballpark' figures for later investigation. MESA and PARSEC, by contrast, are both full stellar evolutionary codes, evolving stars from pre-main sequence to compact remnant. MESA provides information on what is happening in the core as well as on the surface.

3.2. *Combined light, RV and ETV curve analysis with and without joint SED and PARSEC evolutionary track modelling*

We carried out combined, simultaneous analysis of the full *TESS* Cycle 1 light curve data together with the ETV data calculated from both *TESS* and WASP-South light curves for the primary eclipses of both binaries (Section 2.3) and also of the two RV data points derived from the spectroscopic observations (Section 2.6). Several advantages of such a simultaneous analysis are discussed e. g. in Borkovits et al. (2018).

For the analysis we prepared the data sets as follows. We downloaded the calibrated two-minute data files for each sector from the MAST Portal[6]. For the double binary model analysis we detrended the lightcurve with

---

[6] https://mast.stsci.edu/portal/Mashup/Clients/Mast/Portal.html

the software package WōTAN (Hippke et al. 2019). In this way we removed not only any instrumental effects, but also those light curve variations that might have arisen from the rotation and probable chromospheric activities of the targets, but are not relevant for the binary star modelling. Then, to save substantial computational time we binned the two-minute cadence data, averaging them every half hour (1800 s). Finally, we kept only those light curve points that were within the $\pm 0\overset{\text{p}}{.}04$ phase-domain regions around each eclipses. These segments of the light curve were modelled simultaneously with the two ETV curves of the primary eclipses of both binaries (see Section 2.3). Note, some outliers were omitted from the analyzed ETV curves. These points are denoted with an asterix in Table 5 and Table 6.

Finally, we included in the analysis the two RV points (BJD=$2\,458\,760.5678$; RV= $+75.2 \pm 1.8\,\mathrm{km s^{-1}}$, and $2\,458\,761.5605$; $+36.7 \pm 2.2\,\mathrm{km s^{-1}}$).

For our analysis we used software package LIGHTCURVEFACTORY (Borkovits et al. 2018, 2019a). This package is able to model the light- ETV and RV curves of any configurations of eclipsing systems formed by 2–4 stars (i.e. binary, triple and quadruple star systems). For solving the inverse problem, the software employs a Markov chain Monte Carlo (MCMC) parameter search based on an implementation of the generic Metropolis-Hastings algorithm (see e. g. Ford 2005).

In the first stage of the analysis the temperature (T_{A1}) and the mass of the primary (m_{A1}) of binary A were kept fixed on the values given in Section 3.1, while the 21 adjusted parameters were as follows:

(i) 7 light curve related parameters: temperature ratios $(T_2/T_1)_{A,B}$ and T_{Ba}/T_{Aa}; the durations of the two primary eclipses $(\Delta t_{pri})_{A,B}$ (which is closely related to the sum of the fractional radii of the binary stars, see Rappaport et al. 2017 for an explanation); and the ratios of the radii in both binaries $(R_2/R_1)_{A,B}$.

(ii) 2×3 orbital parameters of binaries A and B: we allowed non-zero eccentricities for both binaries and, therefore, $(e \cos \omega)_{A,B}$ and $(e \sin \omega)_{A,B}$ were freely adjusted. The inclinations of the two orbits ($i_{A,B}$) were also adjusted. However, the first sets of runs resulted in insignificantly low inner eccentricites ($e_{A,B} \lesssim 10^{-3}$), so for later runs we assumed circular inner orbits and, therefore, inner eccentricities and arguments of periastrons were no longer adjusted.

(iii) 5 orbital parameters of the outer orbit: period (P_{out}), time of periastron passage τ_{out}, eccentric-

ity and argument of periastron as $(e \cos \omega)_{out}$, $(e \sin \omega)_{out}$ and, finally, the inclination i_{out}.

(iv) 3 mass parameters: the mass ratios of the two binaries ($q_{A,B}$) and the mass of the primary of binary B (m_{B1}).

The two periods ($P_{A,B}$) and reference primary eclipse times ($(T_0)_{A,B}$) of both binaries were not adjusted, but constrained through the ETV curves, as was explained in the Appendix A of Borkovits et al. (2019b). Furthermore, the systemic radial velocity of the center of mass of the whole quadruple system (γ) which in the current model occurs only as an additive parameter independent of any other parameters, was calculated in each trial step by simply minimizing a posteriori the goodness of fit of the RV curve (i.e. χ^2_{RV}).

A logarithmic limb darkening law was applied, interpolating the coefficients at each trial step with the use of the pre-computed passband-dependent tables of the PHOEBE software (Prša & Zwitter 2005).

Computing the orbital motion and therefore, the sky-projected positions of the four bodies, we assumed purely Keplerian orbits. Though the code has an in-built numerical integrator and therefore, numerical integration of the four-body motion, i.e., application of a photodynamical approach could be done easily, we found it unnecessary for the large $P_{out}/P_{A,B}$ ratios which render the four-body perturbations undetectable, at least within the time domain of the available observations.

As a result of this combined analysis we obtained well constrained relative (i.e. dimensionless) stellar parameters (i.e. fractional radii and ratios of temperatures and masses). In order to obtain physical quantities within the frame of a self-consistent model, we added into the analysis the observed cumulative SED of the quadruple, and attempted to find consistent, co-eval PARSEC evolutionary tracks (Bressan et al. 2012) for all the four stars. We generated machine readable PARSEC isochrone tables via the web based tool CMD 3.3[7]. These tables contain theoretically computed fundamental stellar parameters and absolute passband magnitudes in several different photometric systems, for a large three dimensional grid of ages, metallicities and initial stellar masses.

At this final stage of the simultaneous light curve, ETV curves, RV curve, SED and evolutionary track modelling the adjusted parameters have slightly departed from those listed above. First, new adjustable quantities were also introduced, as three independent

---

[7] http://stev.oapd.inaf.it/cgi-bin/cmd
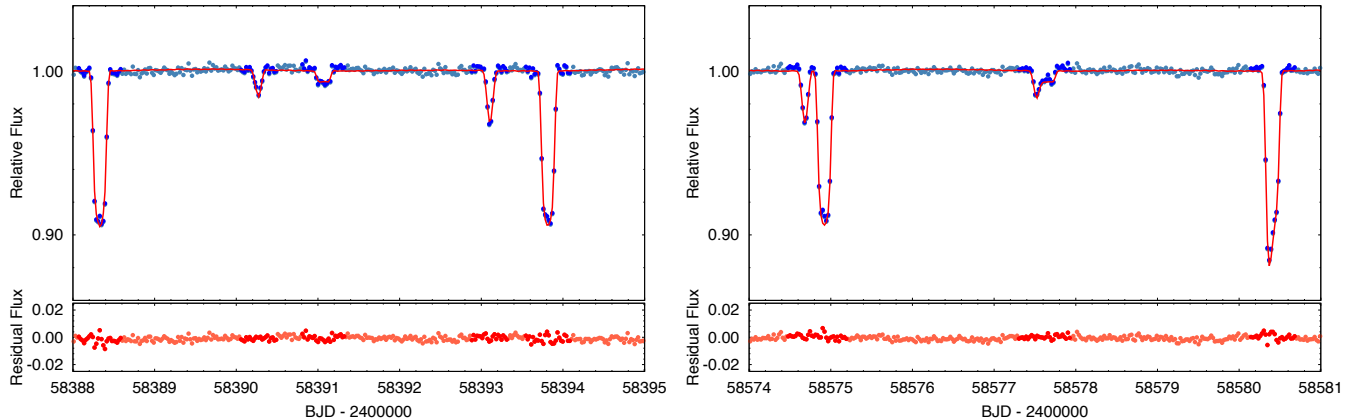
Figure 7. Two 7-day-long sections of the *TESS* Year 1 lightcurve of TIC 278956474. Instead of the full resolution detrended PDCSAP SC flux curve, we plot the 1800-sec binned lightcurve which was used for the photodynamical analysis (see text for details). The dark blue circles in the $\pm 0^{\text{p}}\!.4$ phase-domain around each individual minimum represents the 1800-sec binned flux values used for the photodynamical model, while the other out-of-eclipse data (not used in the modelling) are plotted as light blue circles. The red curve is the cadence-time corrected photodynamical model solution (see Sect. 3.2); the residuals to the model are also shown in the bottom panels. *Left panel:* Here the four different types of eclipses are well separated. From left to right one can see primary eclipse of binary A, secondary of binary B, secondary of binary A, primary of binary B and, finally, the next primary eclipse of binary A. *Right panel* illustrates the superpositions of both the secondary (in the middle) and the primary eclipses (to the right) of the two binaries.

ages of stars Aa, Ab and binary B[8] ($\log \tau_{Aa,Ab,A}$), the metallicity $[M/H]$ of the quadruple, the extinction parameter ($E(B-V)$), and the distance (d) of the system. Furthermore, the mass of the most prominent star Aa was no longer fixed, but allowed to adjust with the use of a simple uniform prior. In this way, the actual stellar masses together with the given stellar ages and metallicity, determined the position of each stars on the `PARSEC` tracks. Then, using a trilinear interpolation with the use of the closest grid points of the precalculated tables, the code interpolated the radii and temperatures of each stars in one hand, and also their absolute passband magnitudes, for the SED fitting, in the other hand. These stellar radii and temperatures were used for the light curve modelling (i. e., in contrast to the first stage, these quantities were no longer adjusted, but constrained instead). Furthermore, the interpolated absolute passband magnitudes transformed into model observed passband magnitudes with the use of the extinction parameter and the system's distance, and then, their sum was compared to the observed magnitudes in each passband. In these final steps, distance (d) was not a free parameter, but was constrained a posteriori in each trial step by minimizing the value of (χ^2_{SED}).

---

[8] In the first round we assumed, as usual, that the four stars have the same age but we were unable to find consistent, co-eval solution. Therefore, we decided to allow different stellar ages. This problem will be discussed later.

A more detailed description of this joint modelling process, including SED fitting with the use of `PARSEC` isochrone tables, can be found in Section 3 of Borkovits et al. (2020).

The results of this comprehensive analysis are tabulated in Table 3 and the model curves are plotted against the observed ETV and light curves in Figs. 4 and 7. Moreover, for a better visualisation of the model light curves of both binaries, we also plot the disentangled, phase-folded, binned, averaged versions of the solution light curve against the similarly processed detrended *TESS* light curves of the binaries in Fig. 3. We tabulate the median values of each parameters together with the 1σ uncertainties. These results will be discussed and compared with an independent SED analysis (Section 3.3) and `MESA` evolutionary tracks in Section 4.

3.3. *Independent SED analysis*

We used the broadband, combined-light spectral energy distribution (SED) of the system, along with the *Gaia* DR2 parallax, iteratively with the global modeling to check for the possibility of any additional sources of light in the system beyond the four eclipsing components, AaAb+BaBb (Fig. 8). This is separate to the analysis described in Section 3.2 and as such provided an independent check on the parameters found. We performed the independent SED modeling with the procedures that Stassun & Torres (2016) developed for EBs, extended here to the case of two EBs simultaneously.

Table 3. Median values of the parameters from the Double EB simultaneous lightcurve and SB1 radial velocity and double ETV and joint SED and PARSEC evolutionary tracks solution. γ is the systemic radial velocity of the quadruple.

Parameter	Binary A		Binary B		Outer orbit
P [days]	$5.488068^{+0.000016}_{-0.000010}$		$5.674256^{+0.000017}_{-0.000030}$		858^{+7}_{-5}
semimajor axis $[R_\odot]$	$15.70^{+0.09}_{-0.17}$		$14.19^{+0.11}_{-0.10}$		543^{+5}_{-6}
i [deg]	$88.97^{+0.16}_{-0.19}$		$89.23^{+0.16}_{-0.08}$		85^{+3}_{-2}
e	0		0		$0.36^{+0.02}_{-0.03}$
ω [deg]	$-$		$-$		299^{+2}_{-2}
$t_{\rm prim\ eclipse}$ [BJD]	$2\,458\,327.9619^{+0.0002}_{-0.0001}$		$2\,458\,330.6870^{+0.0001}_{-0.0002}$		$2\,458\,930^{+5\,a}_{-5}$
γ [km/s]	$-$		$-$		29^{+5}_{-3}
individual stars	A1	A2	B1	B2	
Relative Quantities:					
mass ratio $[q = m_2/m_1]$	$0.357^{+0.009}_{-0.015}$		$0.876^{+0.025}_{-0.049}$		$0.691^{+0.016}_{-0.016}$
fractional radius[b] $[R/a]$	$0.1045^{+0.0018}_{-0.0020}$	$0.0306^{+0.0005}_{-0.0006}$	$0.0477^{+0.0019}_{-0.0023}$	$0.0435^{+0.0015}_{-0.0014}$	
fractional luminosity	0.927	0.010	0.043	0.020	
Physical Quantities:					
$T_{\rm eff}^c$ [K]	6180^{+99}_{-52}	3680^{+84}_{-95}	4472^{+126}_{-137}	3876^{+131}_{-155}	
mass $[M_\odot]$	$1.271^{+0.035}_{-0.046}$	$0.451^{+0.016}_{-0.020}$	$0.634^{+0.022}_{-0.017}$	$0.550^{+0.020}_{-0.023}$	
radius[c] $[R_\odot]$	$1.641^{+0.036}_{-0.046}$	$0.480^{+0.011}_{-0.014}$	$0.674^{+0.026}_{-0.031}$	$0.617^{+0.025}_{-0.024}$	
luminosity[c] $[L_\odot]$	$3.54^{+0.20}_{-0.18}$	$0.038^{+0.004}_{-0.003}$	$0.16^{+0.01}_{-0.01}$	$0.079^{+0.011}_{-0.012}$	
$[M_{\rm bol}]$	$3.40^{+0.06}_{-0.06}$	$8.32^{+0.10}_{-0.10}$	$6.74^{+0.10}_{-0.08}$	$7.53^{+0.18}_{-0.15}$	
$\log g^c$ [cgs]	$4.11^{+0.01}_{-0.01}$	$4.73^{+0.02}_{-0.02}$	$4.58^{+0.04}_{-0.03}$	$4.60^{+0.03}_{-0.03}$	
$\log(\rm age)$ [dex]	$7.00^{+0.03}_{-0.05}$	$7.90^{+0.07}_{-0.07}$	$7.70^{+0.05}_{-0.11}$		
$[M/H]$ [dex]	$-0.37^{+0.10}_{-0.16}$				
$E(B-V)$ [mag]	$0.108^{+0.025}_{-0.012}$				
$(M_V)_{\rm tot}^c$	$3.39^{+0.06}_{-0.06}$				
distance [pc]	958^{+23}_{-23}				

Notes. (a) Time of periastron passage ($\tau_{\rm out}$); (b) Polar radii; (c) Interpolated from the PARSEC isochrones

In brief, a combined-light SED model is calculated from four Kurucz atmospheres (Kurucz 1970, 2013), interpolated to the initial estimate values of the individual stellar $T_{\rm eff}$ and scaled by the initial estimate values of the stellar surface areas ($4\pi R_\star^2$). We assume the metallicity identified in the best fit models, [M/H] $-0.37^{+0.10}_{-0.16}$ dex. The remaining free parameters of the fit are the extinction, A_V, which we limited to the maximum for the line of sight from the dust maps of Schlegel et al. (1998), and the overall flux normalization, $F_{\rm bol,tot}$. We adopted the NUV magnitudes from GALEX (Galaxy Evolution Explorer), $BVgri$ magnitudes from the APASS (The AAVSO Photometric All-Sky Survey) catalog, the JHK_S magnitudes from *2MASS* (Two Micron All Sky Survey), the W1–W4 magnitudes from *WISE* (Wide-field Infrared Survey Explorer), and the $GG_{BP}GRP$ magnitudes from *Gaia*. Together, the available photometry spans the full stellar SED over the wavelength range 0.2–22 μm (see Fig. 8).

The resulting fit is excellent (Fig. 8) with a reduced $\chi^2 = 1.2$ and $A_V = 0.22^{+0.00}_{-0.02}$ (i.e., the maximum permitted A_V for the line of sight from the dust maps of

Schlegel et al. (1998), which is expected for the nominal system distance). The total (unextincted) $F_{\rm bol,tot}$ obtained from the observed photometry, together with the model inferred bolometric luminosity ($L_{\rm bol,tot} \equiv 4\pi\sigma_{\rm SB}\Sigma R_\star^2 T_{\rm eff}^4$), yields an implied photometric distance of 964±13 pc.

This is consistent with the model in Section 3.2 ($d_{\rm model} = 958^{+23}_{-23}$ pc) and confirms that the system is likely to be further away than the uncorrected *Gaia* parallax indicates ($d_{\rm Gaia} = 928 \pm 12$ pc).

4. DISCUSSION

4.1. *Examining the model*

As demonstrated in Section 2.6, by comparison with other work, the age constraints from the Li I EW are 10-50 Myr. The ages (with uncertainties) of Aa, Ba and Bb in Table 3 are consistent with this.

The uncertainties in the masses of the four stars may appear to be remarkably low. The combined analysis described in Section 3.2 returns mass ratios, fractional radii and fractional luminosity, as indicated in Table 3. The mass of one star is required as an input param-
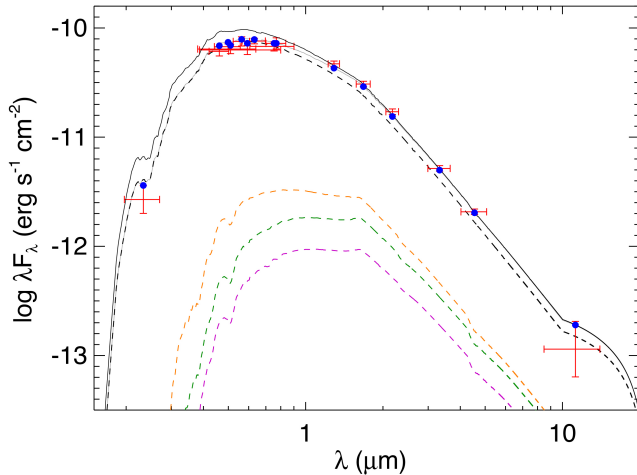
Figure 8. Spectral energy distribution (SED). Red symbols represent the observed photometric measurements, where the horizontal bars represent the effective width of the passband. Blue symbols are the model fluxes from the best-fit combined Kurucz atmosphere model (black solid, without extinction; grey, with extinction). Each of the four stellar components is represented by a Kurucz atmosphere of a different color, scaled by the relative stellar surface areas. Black dashed: Aa. Purple: Ab. Orange: Ba. Green: Bb.

eter. As discussed in Section 3.2, the mass of Aa was allowed to adjust with the use of a simple uniform prior. The uncertainty in the mass of Aa reflects the 'cloud' of solutions which were consistent with the data derived from *TESS* observations, the ETV analysis, the RVs, the SED, data from *Gaia* and the extinction. Stellar evolutionary codes are used to confirm that the age indicated by the physical quantities of the four stars are consistent with the ages indicated by the Li I EW. A wide range of metallicity is indicated, but the stars are clearly sub-solar.

    `PARSEC` evolutionary tracks for the four components of TIC 27895647 from the best fit model are presented in Fig. 9. This $T_{\rm eff}$ vs $\log g$ plot indicates the position of the best fit models, with uncertainties, with color representing age. As indicated in Table 3, the ages are different: Aa is the youngest at $10.0^{+0.7}_{-1.1}$ Myr, Ab the oldest at $79.4^{+13.9}_{-11.8}$ Myr, while Ba and Bb have the same age at $50.1^{+6.2}_{-11.2}$ Myr. Ab is the only star in Table 3 to have an age which is inconsistent with the Li I EW.

    We obtained `MESA` stellar tracks for the minimum, median and maximum masses indicated by the `PARSEC` isochrones at $Z = 0.01$. While this metallicity is not identical to the best fit, it is well within the uncertainty. We match the parameters for Aa at 14 ± 2 Myr, a good approximation with the `PARSEC` tracks given the small difference in metallicity. This is consistent with the Li I EW age.
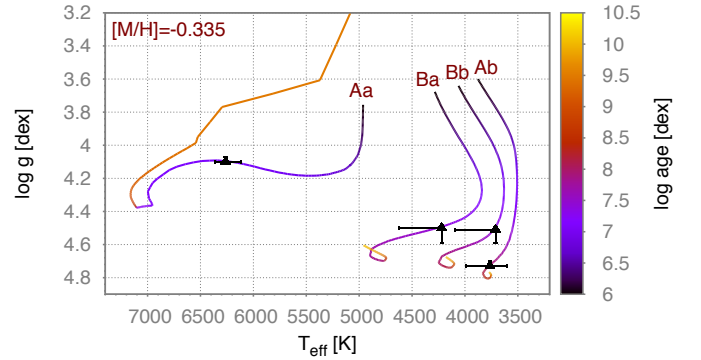
Figure 9. $T_{\rm eff}$ vs $\log g$ PARSEC evolutionary tracks for the four components of TIC 27895647 according to the best fitted model. The color scale denotes the age ($\log \tau$) of the stars at any point along their evolution tracks. Black triangles mark the present locations of the four stars in the solution. We note that these positions, probably unphysically, belong to different ages of the given evolutionary tracks.

    In Fig. 10 we compare properties of stars with an initial mass matching the minimum (green), median (blue) and maximum (red) masses from Table 3. It appears from panel b (core temperature), panel c (core density) and panel d (core pressure), that 14 ± 2 Myr is approximately the point at which a star of the mass and metallicity of Aa would join the main sequence: in other words, Aa is at ZAMS (zero age main sequence). The feature in panel a (radius), where Aa expands and then contracts at 10-20 Myr, is also evident in the `PARSEC` isochrones (Fig. 9), where $T_{\rm eff}$ is plotted against $\log g$. Ab, Ba and Bb would appear to be pre main sequence (PMS) stars.

    The model of Ab is the only one which, from Table 3, does not have an age consistent with the Li I EW. The ratio of radii of Aa and Ab is strongly constrained by the *TESS* data. From panel a in Fig. 10, this points to a lower mass for Ab. Further spectroscopy is required to resolve this issue.

    We see no evidence, such as infrared excess in the SED, of a disc in this system, which would appear to be consistent with Aa being at ZAMS rather than still in the T Tauri phase. Our estimate of E(B-V) is consistent with estimates of $N_{\rm H,tot}$ based on *Swift* data (Section 2.4, Willingale et al. (2013)), although higher than other catalogue values.

4.2. Dynamical properties of the quadruple

    From the joint light curve, ETV and RV analysis TIC 278956474 was found to be one of the most compact known 2+2 quadruple stellar systems. We display the spatial configuration of the system in Fig. 11.
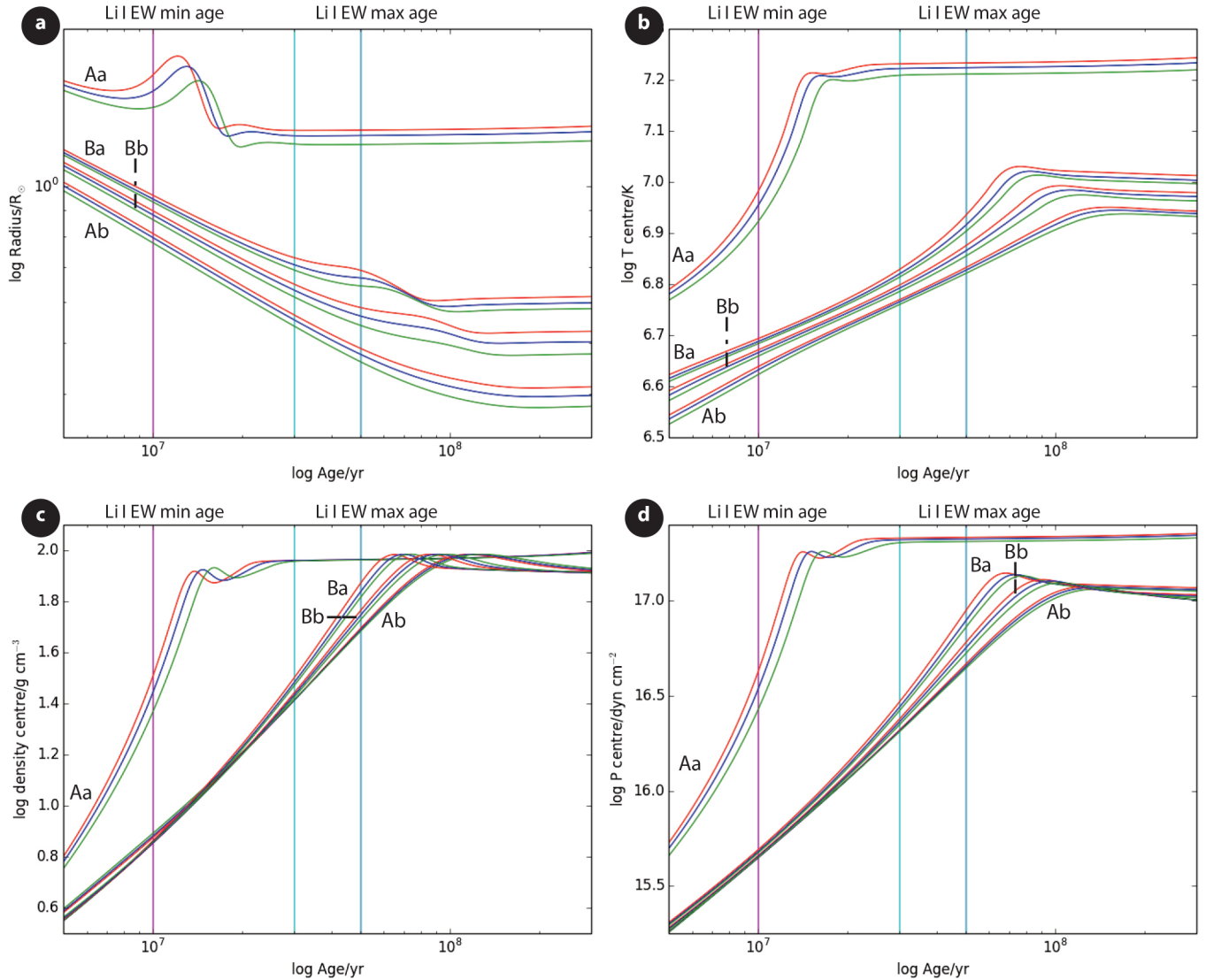
Figure 10. `MESA` isochrones, Z = 0.01, for the median (blue), minimum (green) and maximum (red) masses of the four stars from Table 3. The tracks for each star are labelled in each panel. The Li I EW indicates an age between 10-50 Myr, and these limits are also indicated on each panel, along with an age of 30 Myr. Panel a: stellar radius (log scale) from $0.33 - 2.00$ R$_\odot$; panel b: core temperature; panel c: core density; panel d: core pressure. The point where each star joins the main sequence can be identified from the core characteristics. In these isochrones, which are at a slightly different metallicity to Table 3 (although within the error bars). the median parameters of Aa are matched at an age of 14 ± 2 Myr, at about the same time as, in these stellar tracks, as Aa joins the main sequence.

The median period of the outer orbit was found to be $P_{\mathrm{out}} = 858^{+7}_{-5}$ d, with a moderate eccentricity of $e_{\mathrm{out}} = 0.36^{+0.02}_{-0.03}$. (For comparison, note that the tightest known 2+2 quadruple system, VW LMi, has an outer period of $P_{\mathrm{out}} = 355$ d and eccentricity of $e_{\mathrm{out}} < 0.1$, see Pribulla et al. 2008, 2020.) One should keep in mind, however, that while the bound quadruple nature of the system is certainly beyond question, the quantitative results on the orbital parameters of the outer orbit should be considered only with caution. The reason is, that the *TESS* observations cover only a fraction of an outer or-

bital period and, furthermore, the four former, seasonal WASP minima have large uncertainties. Furthermore, as one can see in Fig. 11, the present solution suggests that the system was observed around the apastron phase of the outer orbit, i.e. when the orbital motion is the slowest and, therefore, the curvatures of ETV curves are also minimized. Therefore, future follow up eclipse timing observations would be extremely useful to obtain more certain outer orbital parameters.

In contrast to the outer orbit, the obtained elements of the two close binary orbits should be robust. The
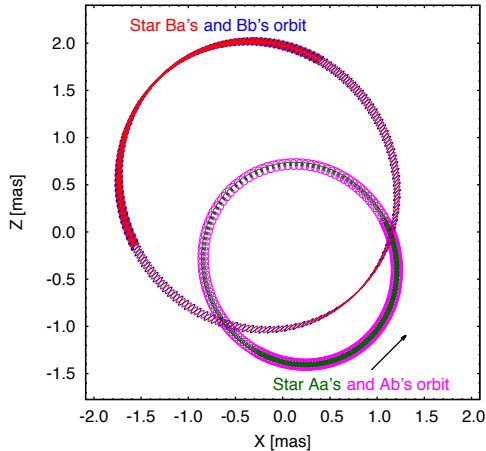
Figure 11. The spatial revolutions of the four members of TIC 278956474, during an outer period, projected to the $X - Z$ plane where the observer is located toward the negative z direction, while the x axis represents the intersection of the orbital plane of the outer orbit with the tangential plane of the sky. The thick arcs represent the four stars' motion during the 11-month-long observations of *TESS* spacecraft. The black arrow shows the direction of the revolution along the outer orbits. The center of mass of the quadruple system is located in the point (0,0). Note, that in the absence of any information about the nodes of the three orbital planes, we assumed quite arbitrarily in this figure that all the three orbital planes intersect the tangential plane of the sky in the same line (i. e. $\Omega_A = \Omega_B = \Omega_{out}$.)

period ratio of the two binary orbits ($P_B/P_A \sim 1.03$) is very close to unity. According to the results of Zasche et al. (2019) there is a significant excess of 2+2 quadruple systems with near equal inner periods, however, the origin of this feature is still unknown (see also Breiter & Vokrouhlický 2018; Tremaine 2020). Turning to the other orbital parameters, as preliminary runs implied that eccentricities of both inner orbits should be less than 0.001, we assumed circular orbits for the further analysis. This assumption does not contradict the young age of the system, as it was shown by Zahn & Bouchet (1989) that the orbits of close binaries formed by late type stars and having period $P \lesssim 7 - 8\,\mathrm{d}$, are expected to circularise by the end of the very first one million years of their pre-MS evolution.

Regarding the binary-binary mutual (gravitational) interactions, their period and amplitude can be estimated from the analytical theory of the perturbations in hierarchical triple systems (see, e. g. Soderhjelm 1975). The key parameter is the period ratio of P_{out}/P_{in} which is ≈ 150 for both binaries. According to the results of Borkovits et al. (2015, 2016) for such a high value, the short term perturbations are negligible and, therefore,

within the time-scale of the $\sim$ 1-yr-long *TESS* observations, the orbital motion of the four stars along their inner and outer orbits can be considered as unperturbed Keplerian motions. As a consequence, neither the *TESS* photometry, nor the RV measurements carry any information about the nodal angles of the three orbital planes and, therefore, despite the fact that the angles of inclination of A ($i_A = 88.97^{+0.16}_{-0.19}$ deg) and B ($i_B = 89.23^{+0.16}_{-0.08}$ deg), and also of the outer orbit ($i_{out} = 85^{+3}_{-2}$ deg) were found to be very similar, one cannot declare that the orbits are almost coplanar. Oppositely, one can say nothing about the mutual inclinations of any two of three orbital planes.[9]

Considering the larger amplitude, so-called apse-node timescale (or, secular) perturbations, their characteristic period is proportional to $P_{out}^2/P_{in} \approx 350\,\mathrm{yr}$ for our quadruple. In such a way, in the case of a non-coplanar configuration, we can expect significant inclination and therefore, well-observable eclipse depth variations within a few decades.

4.3. *Young quadruple systems*

From the Li I EW (Section 2.6), this quadruple system is young (10-50 Myr). In the introduction we referred to Marks & Kroupa (2012), who demonstrated through simulations that if a cluster started with a formal binary fraction of unity, the binary fraction would reduce over time to match presently observed values. Our analysis of this system indicates that even small groupings of stars may form as hierarchical multiples. Whether systems such as TIC 278956474 are likely to become unbound over time would be an interesting follow-up study.

Of the young quadruple systems mentioned in Section 1, some are young enough to be consistent with T Tauri stars. GG Tauri and HD 98800, for example, have evidence of circumbinary discs around one of the inner binaries (Guilloteau et al. 1999; Ribas et al. 2018; Koerner et al. 2000), as well as periods significantly longer than that of TIC 278956474. The inner binaries in GG Tauri have periods of $\approx$ 403 days and 40,000 years (Köhler 2011), while the inner binaries of HD 98800 have periods of about 315 days (Ribas et al. (2018) and references therein). The inner period of HD 34700 has been measured at 23.5 days (Torres 2004; Sterzik et al. 2005). Again, there is evidence of a circumstellar disc (Seok & Li 2015). We have no evidence of a circumstellar disc around TIC 278956474, nor would we expect to find any in a system where the brightest star is at ZAMS.

[9] Strictly speaking what we can obtain uniquely is only $\sin i$, therefore, even these three inclination values are ambiguous for the undetermined signs of $\cos i$-s.

LkCa 3 is a young quadruple system, with an age of about 1.4 Myr (Torres et al. 2013) where all four components are M-class stars. This is interesting as it is generally accepted that high mass stars are more likely to be binary than are low mass stars. Our final model of TIC 278956474 suggests while the spectral classes of the stars will eventually be F3 (Aa), M0 (Ab), K3 (Ba) and K7 (Bb), presently both Ab and Bb could be considered M-class.

González et al. (2006) report the age of AO Vel to be ZAMS, with two short period inner binaries: 1.58 days and 4.15 days. The outer period is reported as 41.0 years. This system is listed on Simbad as an Algol-type eclipsing binary. The inner periods of AO Vel are shorter than those of TIC 278956474, but do not share the characteristic of being very similar in duration.

Wolter et al. (2014) revisited the age of the quadruple system AB Doradus (as opposed to the moving group of the same name), and concludes that it is 50-100 Myr old. This is older than TIC 278956474 and the periods are longer. One inner binary has a period of 11.7 years, the other has a period of 361 days, and the outer period is estimated at $\approx$ 1500 yr (Wolter et al. 2014).

HD 91962 is unusual in that three companions appear to orbit one central star (Tokovinin et al. 2015). The system is considered to be young on the basis of lithium abundances, and the three periods are 170.3 days, 8.85 years and 205 years. Tokovinin et al. (2015) put forward the theory that this system was formed when companions migrated in a dissipative disc formed from the collapse of an isolated core. TIC 278956474 may also have formed from the collapse of an isolated core, but has a more conventional architecture.

HD 86588 is dated to 10 $\lesssim$ Myr $\lesssim$ 150 (Tokovinin et al. 2018) and therefore overlaps in terms of age with TIC 278956474, although not in architecture. The four stars, with masses 1 $\lesssim$ M/M$_\odot$ $\lesssim$ 1.3, are in a three-tier hierarchy. The inner period, 2.4058 days, has not yet fully circularised as the eccentricity is 0.086 $\pm$ 0.003. By contrast, in TIC 278956474 the two inner periods have circularised. Tokovinin et al. (2018) state the outermost period of HD 86588 is around 300 years, and that the intermediate period is 8 years.

Young quadruple systems come in many guises, and TIC 278956474 adds to our understanding of such systems. Both inner periods are known to be short, are circularised and are similar in duration to each other. HD 34700 also has a short inner period. AO Vel also has two short period inner binaries, but one inner period is $\approx$ 2.6 times as long as the other. The inner period of HD 86588 is shorter than in TIC 278956474 but has not yet circularised: both inner periods in TIC 278956474 are al-

ready circular. The other young quadruple systems tend towards longer inner periods.

In terms of architecture, as a 2+2 quadruple system TIC 278956474 is similar to most other known young quadruple systems. Other architectures are observed, but appear to be less common.

Of the eight systems other than TIC 278956474 discussed here, HD 98800 appears to have no entry in *Gaia* DR2, but has a known distance of 47 pc (Soderblom et al. 1998). LkCa3 has no parallax recorded in *Gaia* DR2 but has a known distance of 133 pc (Torres et al. 2013). GG Tauri has a negative parallax in *Gaia* DR2, but has a known distance of 140 pc (Brauer et al. (2019) and references therein). The remaining systems all have reliable parallaxes in *Gaia* DR2. AB Doradus (65.3 $\pm$ 0.1 mas), HD 91962 (28.2 $\pm$ 0.5 mas) and HD 34700 (2.81 $\pm$ 0.05 mas) all have parallaxes indicating they are closer to us than is TIC 278956474. AO Vel (1.12 $\pm$ 0.04 mas) and HD 86588 (1.00 $\pm$ 0.05 mas) have a similar parallax to, and hence are at about the same distance as, TIC 278956474. None appear to be significantly further away.

Because of its magnitude and distance, without *TESS* observations and the SPOC pipeline processing, TIC 278956474's nature as a quadruple system, rather than a single star, would not have been identified.

5. CONCLUSION

The *TESS* mission has enabled the identification of a TIC 278956474 as a 2+2 quadruple system composed of two short-period eclipsing binaries, where all previous observations, including *Gaia*, indicated that this system was one single star.

The eclipses detected in the SPOC pipeline cannot be planetary in nature. Aa and Ab have the same period as each other, as do Ba and Bb. The periods of Aa+Ab and of Ba+Bb, 5.488 days and 5.674 days respectively, would not appear to be consistent with a stable planetary system. While highly inflated short period planets can have secondaries, the eclipses of both Ab and Bb are too deep for this to be a reasonable explanation.

Using SPOC data validation reports, archival WASP-South data, a study of eclipse timing variations, speckle photometry, spectroscopy, data from *Gaia* DR2 and the `BiSEPS`, `MESA` and `PARSEC` stellar evolutionary codes, we identified a model for the four stars in this system which is consistent with observations, the SED and the uncorrected *Gaia* parallax. It is unlikely that there are additional detectable components. The best fit parameters are given in Table 3.

The Li I EW indicates an age of 10-50 Myr, and our model is consistent with this approximation. One star

appears to be at ZAMS, while the other three are still on the PMS.

Further observations, in particular spectroscopy and photometry, would be valuable in refining the properties of this system, in particular the parameters of the outer period (Fig. 11).

ACKNOWLEDGEMENTS

REFERENCES

Aarnio, A. N., Weinberger, A. J., Stassun, K. G., Mamajek, E. E., & James, D. J. 2008, AJ, 136, 2483, doi: 10.1088/0004-6256/136/6/2483

Ahlers, J. P., Kruse, E., Colón, K. D., et al. 2020, ApJ, 888, 63, doi: 10.3847/1538-4357/ab59d0

Andrae, R., Fouesneau, M., Creevey, O., et al. 2018, A&A, 616, A8, doi: 10.1051/0004-6361/201732516

Bailer-Jones, C. A. L., Rybizki, J., Fouesneau, M., Mantelet, G., & Andrae, R. 2018, AJ, 156, 58, doi: 10.3847/1538-3881/aacb21

Baraffe, I., Homeier, D., Allard, F., & Chabrier, G. 2015, A&A, 577, A42, doi: 10.1051/0004-6361/201425481

Bell, C. P. M., Mamajek, E. E., & Naylor, T. 2015, MNRAS, 454, 593, doi: 10.1093/mnras/stv1981

Borkovits, T., Hajdu, T., Sztakovics, J., et al. 2016, MNRAS, 455, 4136, doi: 10.1093/mnras/stv2530

Borkovits, T., Rappaport, S., Hajdu, T., & Sztakovics, J. 2015, MNRAS, 448, 946, doi: 10.1093/mnras/stv015

Borkovits, T., Rappaport, S. A., Hajdu, T., et al. 2020, MNRAS, 493, 5005, doi: 10.1093/mnras/staa495

Borkovits, T., Sperauskas, J., Tokovinin, A., et al. 2019a, MNRAS, 487, 4631, doi: 10.1093/mnras/stz1510

Borkovits, T., Albrecht, S., Rappaport, S., et al. 2018, MNRAS, 478, 5135, doi: 10.1093/mnras/sty1386

Borkovits, T., Rappaport, S., Kaye, T., et al. 2019b, MNRAS, 483, 1934, doi: 10.1093/mnras/sty3157

Brauer, R., Pantin, E., Di Folco, E., et al. 2019, A&A, 628, A88, doi: 10.1051/0004-6361/201935966

Breiter, S., & Vokrouhlický, D. 2018, MNRAS, 475, 5215, doi: 10.1093/mnras/sty132

Bressan, A., Marigo, P., Girardi, L., et al. 2012, MNRAS, 427, 127, doi: 10.1111/j.1365-2966.2012.21948.x

Buckley, D. A. H., Swart, G. P., & Meiring, J. G. 2006, in Proc. SPIE, Vol. 6267, Society of Photo-Optical Instrumentation Engineers (SPIE) Conference Series, 62670Z, doi: 10.1117/12.673750

Chen, Z., Nürnberger, D. E. A., Chini, R., Jiang, Z., & Fang, M. 2015, A&A, 578, A82, doi: 10.1051/0004-6361/201424895

Crause, L. A., Sharples, R. M., Bramall, D. G., et al. 2014, Ground-based and Airborne Instrumentation for Astronomy V, 9147, 91476T, doi: 10.1117/12.2055635

Davis, P. J., Kolb, U., & Willems, B. 2010, Monthly Notices of the Royal Astronomical Society, 403, 179, doi: 10.1111/j.1365-2966.2009.16138.x

Duchêne, G. 1999, A&A, 341, 547. https://arxiv.org/abs/astro-ph/9810507

Farmer, R., Kolb, U., & Norton, A. J. 2013, Monthly Notices of the Royal Astronomical Society, 433, 1133, doi: 10.1093/mnras/stt795

Fausnaugh, M. M., Vallely, P. J., Kochanek, C. S., et al. 2019, arXiv e-prints, arXiv:1904.02171. https://arxiv.org/abs/1904.02171

Ford, E. B. 2005, AJ, 129, 1706, doi: 10.1086/427962

Gaia Collaboration, Prusti, T., de Bruijne, J. H. J., et al. 2016, A&A, 595, A1, doi: 10.1051/0004-6361/201629272

Gaia Collaboration, Brown, A. G. A., Vallenari, A., et al. 2018, A&A, 616, A1, doi: 10.1051/0004-6361/201833051

González, J. F., Hubrig, S., Nesvacil, N., & North, P. 2006, A&A, 449, 327, doi: 10.1051/0004-6361:20054103

González, J. F., Hubrig, S., Nesvacil, N., & North, P. 2008a, in Multiple Stars Across the H-R Diagram, ed. S. Hubrig, M. Petr-Gotzens, & A. Tokovinin, 259, doi: 10.1007/978-3-540-74745-1_33

González, J. F., Nesvacil, N., & Hubrig, S. 2008b, in Precision Spectroscopy in Astrophysics, ed. N. C. Santos, L. Pasquini, A. C. M. Correia, & M. Romaniello, 291–292, doi: 10.1007/978-3-540-75485-5_69

Guilloteau, S., Dutrey, A., & Simon, M. 1999, A&A, 348, 570

Güver, T., & Özel, F. 2009, MNRAS, 400, 2050, doi: 10.1111/j.1365-2966.2009.15598.x

Hełminiak, K. G., Ukita, N., Kambe, E., et al. 2017, A&A, 602, A30, doi: 10.1051/0004-6361/201630379

Hippke, M., David, T. J., Mulders, G. D., & Heller, R. 2019, AJ, 158, 143, doi: 10.3847/1538-3881/ab3984

Holoien, T. W. S., Vallely, P. J., Auchettl, K., et al. 2019, ApJ, 883, 111, doi: 10.3847/1538-4357/ab3c66

Huber, D., Chaplin, W. J., Chontos, A., et al. 2019, AJ, 157, 245, doi: 10.3847/1538-3881/ab1488

Janson, M., Brandner, W., Lenzen, R., et al. 2007, A&A, 462, 615, doi: 10.1051/0004-6361:20066208

Jayawardhana, R., Luhman, K. L., D'Alessio, P., & Stauffer, J. R. 2002, ApJL, 571, L51, doi: 10.1086/341202

Jenkins, J. M. 2019, in American Astronomical Society Meeting Abstracts, Vol. 233, American Astronomical Society Meeting Abstracts #233, 423.02

Jenkins, J. M., Twicken, J. D., McCauliff, S., et al. 2016, in Society of Photo-Optical Instrumentation Engineers (SPIE) Conference Series, Vol. 9913, Proc. SPIE, 99133E, doi: 10.1117/12.2233418

Kniazev, A. Y., Gvaramadze, V. V., & Berdnikov, L. N. 2016, Monthly Notices of the Royal Astronomical Society, 459, 3068, doi: 10.1093/mnras/stw889

Kniazev, A. Y., Gvaramadze, V. V., & Berdnikov, L. N. 2017, in Stars: From Collapse to Collapse, Vol. 510, eprint: arXiv:1612.00292, 480

Koerner, D. W., Jensen, E. L. N., Cruz, K. L., Guild, T. B., & Gultekin, K. 2000, ApJL, 533, L37, doi: 10.1086/312593

Köhler, R. 2011, A&A, 530, A126, doi: 10.1051/0004-6361/201016327

Kraus, A. L., Shkolnik, E. L., Allers, K. N., & Liu, M. C. 2014, AJ, 147, 146, doi: 10.1088/0004-6256/147/6/146

Kurucz, R. L. 1970, SAO Special Report, 309

—. 2013, ATLAS12: Opacity sampling model atmosphere program. http://ascl.net/1303.024

Lallement, R., Babusiaux, C., Vergely, J. L., et al. 2019, VizieR Online Data Catalog, J/A+A/625/A135

Lee, C. U., Kim, S. L., Lee, J. W., et al. 2008, MNRAS, 389, 1630, doi: 10.1111/j.1365-2966.2008.13708.x

Li, J., Tenenbaum, P., Twicken, J. D., et al. 2019, PASP, 131, 024506, doi: 10.1088/1538-3873/aaf44d

Marks, M., & Kroupa, P. 2012, Astronomy and Astrophysic, 543, A8, doi: 10.1051/0004-6361/201118231

Mentuch, E., Brandeker, A., van Kerkwijk, M. H., Jayawardhana, R., & Hauschildt, P. H. 2008, ApJ, 689, 1127, doi: 10.1086/592764

Morris, R. L., Twicken, J. D., Smith, J. C., et al. 2017, Kepler Data Processing Handbook: Photometric Analysis, Kepler Science Document

Paxton, B., Bildsten, L., Dotter, A., et al. 2011, The Astrophysical Journal Supplement Series, 192, 3, doi: 10.1088/0067-0049/192/1/3

Paxton, B., Cantiello, M., Arras, P., et al. 2013, The Astrophysical Journal Supplement Series, 208, 4, doi: 10.1088/0067-0049/208/1/4

Paxton, B., Marchant, P., Schwab, J., et al. 2015, The Astrophysical Journal Supplement Series, 220, 15, doi: 10.1088/0067-0049/220/1/15

Pollacco, D. L., Skillen, I., Collier Cameron, A., et al. 2006, PASP, 118, 1407, doi: 10.1086/508556

Pribulla, T., Baluďanský, D., Dubovský, P., et al. 2008, MNRAS, 390, 798, doi: 10.1111/j.1365-2966.2008.13781.x

Pribulla, T., Puha, E., Borkovits, T., et al. 2020, MNRAS, 494, 178, doi: 10.1093/mnras/staa699

Prša, A., & Zwitter, T. 2005, ApJ, 628, 426, doi: 10.1086/430591

Raghavan, D., McAlister, H. A., Henry, T. J., et al. 2010, ApJS, 190, 1, doi: 10.1088/0067-0049/190/1/1

Rappaport, S., Vanderburg, A., Borkovits, T., et al. 2017, MNRAS, 467, 2160, doi: 10.1093/mnras/stx143

Ribas, Á., Macías, E., Espaillat, C. C., & Duchêne, G. 2018, ApJ, 865, 77, doi: 10.3847/1538-4357/aad81b

Ricker, G. R., Vanderspek, R. K., Latham, D. W., & Winn, J. N. 2014, in American Astronomical Society Meeting Abstracts, Vol. 224, American Astronomical Society Meeting Abstracts #224, 113.02

Riedel, A. R., Blunt, S. C., Lambrides, E. L., et al. 2017, AJ, 153, 95, doi: 10.3847/1538-3881/153/3/95

Riello, M., De Angeli, F., Evans, D. W., et al. 2018, A&A, 616, A3, doi: 10.1051/0004-6361/201832712

Schlafly, E. F., & Finkbeiner, D. P. 2011, ApJ, 737, 103, doi: 10.1088/0004-637X/737/2/103

Schlegel, D. J., Finkbeiner, D. P., & Davis, M. 1998, ApJ, 500, 525, doi: 10.1086/305772

Schofield, M., Chaplin, W. J., Huber, D., et al. 2019, ApJS, 241, 12, doi: 10.3847/1538-4365/ab04f5

Schönrich, R., McMillan, P., & Eyer, L. 2019, MNRAS, 487, 3568, doi: 10.1093/mnras/stz1451

Seok, J. Y., & Li, A. 2015, ApJ, 809, 22, doi: 10.1088/0004-637X/809/1/22

Shkolnik, E. L., Allers, K. N., Kraus, A. L., Liu, M. C., & Flagg, L. 2017, AJ, 154, 69, doi: 10.3847/1538-3881/aa77fa

Soderblom, D. R., King, J. R., Siess, L., et al. 1998, ApJ, 498, 385, doi: 10.1086/305542

Soderhjelm, S. 1975, A&A, 42, 229

Stassun, K. G., & Torres, G. 2016, AJ, 152, 180, doi: 10.3847/0004-6256/152/6/180

—. 2018, ApJ, 862, 61, doi: 10.3847/1538-4357/aacafc

Sterzik, M. F., Melo, C. H. F., Tokovinin, A. A., & van der Bliek, N. 2005, A&A, 434, 671, doi: 10.1051/0004-6361:20042302

Tokovinin, A. 2018, PASP, 130, 035002, doi: 10.1088/1538-3873/aaa7d9

Tokovinin, A., Corbett, H., Fors, O., et al. 2018, AJ, 156, 120, doi: 10.3847/1538-3881/aad694

Tokovinin, A., Latham, D. W., & Mason, B. D. 2015, AJ, 149, 195, doi: 10.1088/0004-6256/149/6/195

Tokovinin, A. A. 1999, Astronomy Letters, 25, 669

Torres, G. 2004, AJ, 127, 1187, doi: 10.1086/381066

Torres, G., Ruíz-Rodríguez, D., Badenas, M., et al. 2013, ApJ, 773, 40, doi: 10.1088/0004-637X/773/1/40

Tremaine, S. 2020, MNRAS, 493, 5583, doi: 10.1093/mnras/staa643

Twicken, J. D., Clarke, B. D., Bryson, S. T., et al. 2010, Society of Photo-Optical Instrumentation Engineers (SPIE) Conference Series, Vol. 7740, Photometric analysis in the Kepler Science Operations Center pipeline, 774023, doi: 10.1117/12.856790

Twicken, J. D., Catanzarite, J. H., Clarke, B. D., et al. 2018, PASP, 130, 064502, doi: 10.1088/1538-3873/aab694

Udalski, A., Szymański, M. K., & Szymański, G. 2015, AcA, 65, 1. https://arxiv.org/abs/1504.05966

Willems, B., & Kolb, U. 2002, Monthly Notice of the Royal Astronomical Society, 337, 1004, doi: 10.1046/j.1365-8711.2002.05985.x

—. 2004, Astronomy and Astrophysics, 419, 1057, doi: 10.1051/0004-6361:20040085

Willems, B., Kolb, U., & Justham, S. 2006, Monthly Notices of the Royal Astronomical Society, 367, 1103, doi: 10.1111/j.1365-2966.2006.10041.x

Willingale, R., Starling, R. L. C., Beardmore, A. P., Tanvir, N. R., & O'Brien, P. T. 2013, MNRAS, 431, 394, doi: 10.1093/mnras/stt175

Wolter, U., Czesla, S., Fuhrmeister, B., et al. 2014, A&A, 570, A95, doi: 10.1051/0004-6361/201424137

Zahn, J. P., & Bouchet, L. 1989, A&A, 223, 112

Zasche, P., & Uhlař, R. 2016, A&A, 588, A121, doi: 10.1051/0004-6361/201628153

Zasche, P., Vokrouhlický, D., Wolf, M., et al. 2019, A&A, 630, A128, doi: 10.1051/0004-6361/201936328

Zhan, Z., Günther, M. N., Rappaport, S., et al. 2019, ApJ, 876, 127, doi: 10.3847/1538-4357/ab158c

Ziegler, C., Tokovinin, A., Briceño, C., et al. 2020, AJ, 159, 19, doi: 10.3847/1538-3881/ab55e9

APPENDIX

SPOC data

APPENDIX

ETV tables

Table 4. Data from SPOC. The secondary in component Aa coincides with the time of the primary in component Ab, and vice versa. Similarly for components Ba and Bb. Secondary depths are therefore only included where each component is not separately identified. A second science run was completed for multisector 1-13 in order to identify component Ab at the correct period and to remove the partial eclipse of Aa at the end of sector 8. This science run is identified as sector 1-13*.

Component	Sector	Period/days	Depth/ppm	Duration/hr	Ingress/hr	Odd depth/ppm	Even depth/ppm	Secondary depth/ppm
Aa	1	5.4881 ± 0.0002	94800 ± 900	5.50 ± 0.04	1.22 ± 0.04	94000 ± 1000	96000 ± 1000	Component Ab
Aa	1-2	5.48797 ± 0.00008	94600 ± 600	5.44 ± 0.03	1.21 ± 0.02	95100 ± 900	94500 ± 800	Component Ab
Aa	1-3	5.48789 ± 0.00004	94200 ± 500	5.43 ± 0.02	1.21 ± 0.02	93900 ± 600	94500 ± 600	Component Ab
Aa	1-6	5.48797 ± 0.00002	93900 ± 300	5.41 ± 0.01	1.20 ± 0.01	95700 ± 500	92900 ± 500	Component Ab
Aa	1-9	5.487995 ± 0.000008	94200 ± 300	5.43 ± 0.01	1.21 ± 0.01	94400 ± 400	94000 ± 400	Component Ab
Aa	1-13	5.488035 ± 0.000005	93900 ± 200	5.43 ± 0.01	1.22 ± 0.01	94600 ± 300	93300 ± 300	8900 ± 400
Aa	1-13*	5.488036 ± 0.000005	93900 ± 200	5.43 ± 0.01	1.22 ± 0.01	94500 ± 300	93400 ± 300	Component Ab
Aa	2	5.4878 ± 0.0002	94700 ± 900	5.42 ± 0.03	1.22 ± 0.03	94000 ± 1000	97000 ± 2000	Component Ab
Aa	3	5.4882 ± 0.0003	93700 ± 600	5.43 ± 0.03	1.20 ± 0.03	94300 ± 800	92400 ± 900	Component Ab
Aa	4	5.4882 ± 0.0003	93400 ± 800	5.34 ± 0.04	1.18 ± 0.04	98000 ± 1000	91000 ± 1000	Component Ab
Aa	5	5.4884 ± 0.0003	94300 ± 800	5.47 ± 0.03	1.24 ± 0.03	94000 ± 1000	95000 ± 1000	Component Ab
Aa	6	5.4881 ± 0.0003	95700 ± 800	5.41 ± 0.03	1.21 ± 0.03	96000 ± 1000	96000 ± 1000	Component Ab
Aa	7	5.4877 ± 0.0002	93000 ± 1000	5.38 ± 0.04	1.21 ± 0.03	88000 ± 2000	97000 ± 2000	7000 ± 2000
Aa	8	5.4873 ± 0.0002	93000 ± 1000	5.46 ± 0.03	1.21 ± 0.03	56378 ± 1000	95147 ± 2000	Component Ab
Aa	9	5.4888 ± 0.0003	93400 ± 900	5.45 ± 0.03	1.27 ± 0.03	94000 ± 1000	93293 ± 1000	Component Ab
Aa	10	5.4890 ± 0.0003	93600 ± 700	5.53 ± 0.04	1.31 ± 0.04	98000 ± 1000	90000 ± 1000	Component Ab
Aa	11	5.4885 ± 0.0003	92100 ± 800	5.41 ± 0.04	1.20 ± 0.04	91000 ± 1000	93000 ± 1000	Component Ab
Aa	12	5.4880 ± 0.0003	95000 ± 1000	5.42 ± 0.04	1.2 ± 0.04	95000 ± 2000	94000 ± 2000	Component Ab
Aa	13	5.4882 ± 0.0003	94000 ± 1000	5.43 ± 0.04	1.21 ± 0.04	94000 ± 2000	94000 ± 2000	8000 ± 2000
Ab	1	5.495 ± 0.003	8500 ± 800	5.5 ± 0.4	1.1 ± 0.4	8000 ± 30000	8000 ± 1000	Component Aa
Ab	1-2	5.4883 ± 0.0008	9100 ± 600	5.3 ± 0.2	1.1 ± 0.2	8900 ± 800	8300 ± 800	Component Aa
Ab	1-3	5.4881 ± 0.0004	9100 ± 400	5.3 ± 0.2	1.0 ± 0.2	9400 ± 500	8200 ± 600	Component Aa
Ab	1-6	5.4882 ± 0.0001	9000 ± 300	5.3 ± 0.1	0.9 ± 0.1	9300 ± 400	8400 ± 400	Component Aa
Ab	1-9	5.48809 ± 0.00007	8900 ± 200	5.4 ± 0.1	1.1 ± 0.1	9200 ± 300	8600 ± 400	Component Aa
Ab	1-13	2.74403 ± 0.00002	8900 ± 200	5.29 ± 0.09	1.0 ± 0.1	Model fitter failed	Model fitter failed	n/a
Ab	1-13*	5.48808 ± 0.00004	8900 ± 200	5.29 ± 0.08	1.0 ± 0.1	9000 ± 300	8700 ± 300	Component Aa
Ab	2	5.488 ± 0.002	9700 ± 700	5.2 ± 0.2	1.0 ± 0.3	9900 ± 900	9000 ± 1000	Component Aa
Ab	3	10.977 ± 0.004	9155 ± 600	5.0 ± 0.3	0.4 ± 0.3	9600 ± 900	8700 ± 900	Component Aa
Ab	4	5.482 ± 0.002	7700 ± 700	4.9 ± 0.3	0.4 ± 0.3	8000 ± 1000	8000 ± 1000	Component Aa
Ab	5	5.488 ± 0.002	9500 ± 600	5.5 ± 0.2	1.4 ± 0.3	8200 ± 700	10100 ± 800	Component Aa
Ab	6	5.489 ± 0.002	9600 ± 700	4.9 ± 0.2	0.6 ± 0.2	10000 ± 1000	9000 ± 1000	Component Aa
Ab	8	5.492 ± 0.002	7600 ± 900	4.2 ± 0.3	0.4 ± 0.3	8000 ± 1000	8000 ± 800	Component Aa
Ab	9	5.489 ± 0.001	8900 ± 600	5.1 ± 0.2	0.4 ± 0.2	9300 ± 700	8500 ± 800	Component Aa
Ab	10	$5.488 /pm 0.002$	9002 ± 700	5.1 ± 0.3	0.8 ± 0.3	9500 ± 700	7000 ± 1000	Component Aa
Ab	11	5.485 ± 0.001	8000 ± 500	5.0 ± 0.3	0.6 ± 0.3	8400 ± 800	800 ± 800	Component Aa
Ab	12	5.485 ± 0.002	9600 ± 800	5.0 ± 0.3	0.8 ± 0.3	10000 ± 1000	10000 ± 1000	Component Aa
B	1-6	2.83721 ± 0.00002	26000 ± 300	3.34 ± 0.04	1.67 ± 0.02	16700 ± 400	33900 ± 400	n/a
B	1-9	2.83718 ± 0.00001	25400 ± 300	3.34 ± 0.04	1.67 ± 0.02	16700 ± 300	33500 ± 300	n/a
B	1-13	2.837163 ± 0.000007	25100 ± 200	3.34 ± 0.03	1.67 ± 0.02	16400 ± 300	33400 ± 300	n/a
B	1-13*	2.837162 ± 0.000007	25100 ± 200	3.34 ± 0.03	1.67 ± 0.02	16400 ± 200	33400 ± 300	n/a
B	3	2.8372 ± 0.0004	28400 ± 700	3.3 ± 0.1	1.65 ± 0.05	34400 ± 900	17000 ± 1000	n/a
B	4	2.8366 ± 0.0004	23700 ± 800	3.3 ± 0.1	1.63 ± 0.06	18600 ± 900	33000 ± 1000	n/a
B	5	2.8373 ± 0.0003	26500 ± 600	3.31 ± 0.08	1.65 ± 0.04	33800 ± 700	15800 ± 800	n/a
B	8	2.8370 ± 0.0003	23000 ± 1000	3.4 ± 0.1	1.71 ± 0.06	31000 ± 1000	17000 ± 1000	n/a
B	9	2.8369 ± 0.0003	23400 ± 700	3.3 ± 0.1	1.66 ± 0.05	16600 ± 900	32600 ± 900	n/a
B	11	2.8371 ± 0.0003	23800 ± 700	3.3 ± 0.1	1.63 ± 0.05	32300 ± 800	16400 ± 900	n/a
Ba	1	5.6742 ± 0.0009	37000 ± 1000	3.4 ± 0.1	1.70 ± 0.05	39000 ± 2000	34000 ± 2000	15000 ± 1000
Ba	1-2	5.6744 ± 0.0002	35000 ± 700	3.32 ± 0.07	1.66 ± 0.04	36800 ± 900	33000 ± 2000	Component Bb
Ba	1-3	5.6744 ± 0.0001	34700 ± 500	3.29 ± 0.06	1.65 ± 0.03	35600 ± 700	33600 ± 800	Component Bb
Ba	2	5.6742 ± 0.0007	33000 ± 1000	3.21 ± 0.09	1.60 ± 0.04	33000 ± 1000	34000 ± 1000	Component Bb
Ba	6	5.6745 ± 0.0007	32600 ± 900	3.38 ± 0.09	1.69 ± 0.05	33000 ± 2000	33000 ± 1000	Component Bb
Ba	7	5.6736 ± 0.0007	33000 ± 1000	3.3 ± 0.1	1.64 ± 0.05	33000 ± 1000	34000 ± 1000	Component Bb
Ba	12	5.6740 ± 0.0008	36000 ± 1000	3.3 ± 0.1	1.67 ± 0.05	35000 ± 2000	36000 ± 2000	Component Bb
Ba	13	5.671 ± 0.0008	34000 ± 1000	3.3 ± 0.1	1.65 ± 0.06	36000 ± 2000	33000 ± 2000	2300 ± 900
Bb	1-2	5.6742 ± 0.0006	15800 ± 600	3.3 ± 0.2	1.64 ± 0.08	15000 ± 1000	16600 ± 900	Component Ba
Bb	1-3	5.6747 ± 0.0003	16000 ± 600	3.4 ± 0.2	1.67 ± 0.07	15000 ± 1000	16600 ± 700	Component Ba
Bb	2	5.675 ± 0.001	14900 ± 900	3.3 ± 0.2	1.64 ± 0.1	16000 ± 2000	14000 ± 1000	Component Ba
Bb	6	5.675 ± 0.001	16500 ± 700	3.3 ± 0.2	1.66 ± 0.09	18000 ± 1000	15000 ± 1000	Component Ba
Bb	7	2.836 ± 0.003	15000 ± 2000	3.3 ± 0.3	1.6 ± 0.2	Model fitter failed	Model fitter failed	n/a
Bb	10	5.6754 ± 0.0009	15400 ± 800	3.2 ± 0.2	1.6 ± 0.1	17000 ± 1000	14000 ± 1000	2331.4 ± 600
Bb	12	5.6724 ± 0.0001	17000 ± 1000	3.1 ± 0.2	1.5 ± 0.1	15000 ± 2000	18000 ± 2000	Component Ba

Table 5. Times of minima of TIC 278956474A. The first four items give seasonal minima deduced from WASP-South observations. Other data refer to individual eclipses observed by *TESS* spacecraft. Integer and half-integer cycle numbers refer to primary and secondary eclipses. For the ETV analysis, discussed in the main part of the paper, only primary eclipses were used. Five primary eclipses marked with asterisks were omitted from the analysis as outliers.

BJD −2 400 000	Cycle no.	std. dev. (d)	BJD −2 400 000	Cycle no.	std. dev. (d)	BJD −2 400 000	Cycle no.	std. dev. (d)
54826.636808	-638.0	0.000549	58445.944896	21.5	0.001468	58572.167299	44.5	0.000979
55194.333657	-571.0	0.001098	58448.697063	22.0	0.000144	58574.921743	45.0	0.000141
55562.031003	-504.0	0.001098	58454.185939*	23.0	0.000128	58577.656449	45.5	0.000872
55924.227778	-438.0	0.001098	58456.919263	23.5	0.001334	58580.409879	46.0	0.000133
58327.962429	0.0	0.000174	58459.673021	24.0	0.000130	58585.899280*	47.0	0.000168
58330.700768	0.5	0.002383	58462.411516	24.5	0.002015	58588.633820	47.5	0.001724
58333.449810	1.0	0.000223	58470.649037	26.0	0.000121	58591.386912	48.0	0.000130
58336.192167	1.5	0.001068	58473.389849	26.5	0.001229	58594.119542	48.5	0.000951
58341.672992	2.5	0.002330	58476.136447	27.0	0.000126	58599.627581	49.5	0.004254
58344.425319	3.0	0.000195	58478.879249	27.5	0.001043	58602.362426	50.0	0.000175
58347.162986	3.5	0.001927	58481.624776	28.0	0.000129	58605.100888	50.5	0.001569
58349.913744	4.0	0.000150	58484.363435	28.5	0.000751	58607.850858	51.0	0.000153
58352.658427	4.5	0.003649	58487.112762	29.0	0.000132	58613.338684	52.0	0.000178
58355.401627	5.0	0.000131	58489.871693	29.5	0.001835	58616.075255	52.5	0.001549
58358.135368	5.5	0.000848	58492.600453	30.0	0.000156	58618.827111	53.0	0.000147
58360.890011	6.0	0.000140	58495.332830	30.5	0.001338	58621.561695	53.5	0.002102
58363.626999	6.5	0.000658	58498.091166*	31.0	0.000114	58627.044601	54.5	0.001205
58366.377135	7.0	0.000161	58500.833321	31.5	0.001364	58629.803406	55.0	0.000155
58369.122007	7.5	0.001326	58506.312484	32.5	0.001090	58632.542077	55.5	0.000921
58371.864689	8.0	0.000139	58509.064706	33.0	0.000139	58635.290572	56.0	0.000146
58374.600726	8.5	0.001342	58511.819107	33.5	0.001813	58638.019856	56.5	0.001641
58377.352284	9.0	0.000176	58514.552784	34.0	0.000109	58640.779257	57.0	0.000178
58380.083629	9.5	0.001641	58520.041266	35.0	0.000131	58643.516085	57.5	0.001110
58388.328366	11.0	0.000168	58522.785816	35.5	0.001032	58646.267602	58.0	0.000178
58391.068826	11.5	0.001415	58525.529251	36.0	0.000152	58648.989799	58.5	0.001197
58393.816827	12.0	0.000204	58528.268281	36.5	0.001249	58651.755432	59.0	0.000158
58399.305162	13.0	0.000119	58536.507117*	38.0	0.000140	58654.489005	59.5	0.001140
58402.042463	13.5	0.002526	58539.236620	38.5	0.002777	58657.244598	60.0	0.000171
58404.792220	14.0	0.000199	58541.983305*	39.0	0.000730	58659.983219	60.5	0.000950
58413.012446	15.5	0.001254	58544.732586	39.5	0.001435	58662.733098	61.0	0.000206
58415.768382	16.0	0.000163	58547.480518	40.0	0.000138	58665.481953	61.5	0.001844
58426.744932	18.0	0.000142	58550.226769	40.5	0.002788	58670.967933	62.5	0.001479
58429.484915	18.5	0.004152	58552.968752	41.0	0.000133	58673.708794	63.0	0.000138
58432.234014*	19.0	0.000134	58558.457413	42.0	0.000118	58676.450537	63.5	0.001335
58434.963124	19.5	0.002461	58561.201168	42.5	0.001212	58679.197053	64.0	0.000169
58440.456132	20.5	0.001355	58563.945780	43.0	0.000125	58681.947227	64.5	0.001120
58443.208790	21.0	0.000129	58566.683307	43.5	0.001859			

Table 6. Times of minima of TIC 278956474B. Integer and half-integer cycle numbers refer to primary and secondary eclipses. For the ETV analysis, discussed in the main part of the paper, only primary eclipses were used. Primary eclipses marked with asteriskswere omitted from the analysis as outliers.

BJD −2 400 000	Cycle no.	std. dev. (d)	BJD −2 400 000	Cycle no.	std. dev. (d)	BJD −2 400 000	Cycle no.	std. dev. (d)
58327.851141	-0.5	0.001078	58452.679392	21.5	0.001835	58571.848064	42.5	0.004826
58330.686768	0.0	0.000472	58455.526205	22.0	0.000464	58574.684476	43.0	0.000540
58333.528644	0.5	0.024207	58458.360384	22.5	0.001879	58577.518764	43.5	0.000973
58336.361373	1.0	0.000515	58461.196935*	23.0	0.000365	58580.356649	44.0	0.000601
58342.033623*	2.0	0.000564	58464.050752	23.5	0.084498	58586.031380	45.0	0.000574
58344.876998	2.5	0.001018	58469.709234	24.5	0.000666	58588.873801	45.5	0.001518
58347.706677*	3.0	0.001567	58472.547953	25.0	0.000955	58591.706607	46.0	0.000473
58350.555515	3.5	0.001240	58475.388524	25.5	0.000929	58594.549605	46.5	0.000516
58356.227407	4.5	0.000779	58478.217404*	26.0	0.000962	58600.216707	47.5	0.001307
58359.060381	5.0	0.000372	58481.055791	26.5	0.001051	58603.056249	48.0	0.000425
58361.901701	5.5	0.000839	58483.891625*	27.0	0.000601	58605.887612	48.5	0.000994
58364.732752	6.0	0.000722	58486.738529	27.5	0.001463	58608.722728*	49.0	0.000537
58370.408184	7.0	0.000478	58489.570680	28.0	0.000380	58614.401286	50.0	0.000479
58373.248194	7.5	0.001198	58492.406297	28.5	0.001592	58617.242303	50.5	0.001257
58376.082783	8.0	0.000501	58495.246523	29.0	0.000561	58620.073963*	51.0	0.000724
58378.922654	8.5	0.001383	58498.085931	29.5	0.000965	58622.913595	51.5	0.001044
58387.429007*	10.0	0.000441	58500.914410*	30.0	0.000567	58625.754045	52.0	0.000944
58390.269093	10.5	0.003915	58506.594229	31.0	0.000351	58628.598291	52.5	0.001760
58393.105081	11.0	0.000456	58509.437963	31.5	0.001246	58631.428199	53.0	0.000505
58398.781892	12.0	0.000383	58512.267718	32.0	0.000517	58634.269473	53.5	0.001228
58401.621516	12.5	0.001218	58515.106161	32.5	0.000786	58637.101893	54.0	0.000492
58404.454889	13.0	0.000390	58517.935775*	33.0	0.000618	58642.776264	55.0	0.000615
58412.965130	14.5	0.001871	58520.781624	33.5	0.001152	58645.618682	55.5	0.000989
58415.799460*	15.0	0.000477	58523.616511	34.0	0.000617	58648.446307	56.0	0.000439
58421.478895	16.0	0.002228	58526.449138	34.5	0.000690	58651.283550	56.5	0.001568
58427.152712	17.0	0.000595	58537.802322	36.5	0.001126	58654.122005	57.0	0.000305
58429.994122	17.5	0.001210	58540.637289	37.0	0.000328	58656.962553	57.5	0.001599
58432.827096	18.0	0.000552	58546.311254	38.0	0.000428	58659.797199	58.0	0.001004
58435.667600	18.5	0.000915	58549.151810	38.5	0.000682	58662.627503	58.5	0.001251
58438.498776*	19.0	0.000330	58551.986126	39.0	0.000410	58665.470728	59.0	0.000598
58441.334196	19.5	0.001504	58554.816386	39.5	0.001820	58671.145005	60.0	0.000736
58444.173601*	20.0	0.000600	58560.498489	40.5	0.000809	58673.988971	60.5	0.001242
58447.015592	20.5	0.001109	58563.336764	41.0	0.000548	58676.819757	61.0	0.000798
58449.850482	21.0	0.000593	58566.164903	41.5	0.001345	58679.659708	61.5	0.002367